3-D Medical Image Interpolation Based on Context Classification

3-D MEDICAL IMAGE INTERPOLATION BASED ON CONTEXT CLASSIFICATION

BY

SAHAR ALIPOUR KASHI, B.Sc.

A THESIS
SUBMITTED TO THE DEPARTMENT OF ELECTRICAL & COMPUTER ENGINEERING
AND THE SCHOOL OF GRADUATE STUDIES
OF MCMASTER UNIVERSITY
IN PARTIAL FULFILMENT OF THE REQUIREMENTS
FOR THE DEGREE OF
MASTER OF APPLIED SCIENCE

Master of Applied Science (2010)
(Electrical & Computer Engineering)

McMaster University
Hamilton, Ontario, Canada

TITLE: 3-D Medical Image Interpolation Based on Context Classification

AUTHOR: Sahar Alipour Kashi
B.Sc., (Electrical Engineering)
Isfahan University of Technology, Isfahan, Iran

SUPERVISOR: Dr. Shahram Shirani
Dr. Xiaolin Wu

NUMBER OF PAGES: xi, 54

To those who were always there when I needed them

Abstract

This thesis is concerned with interpolation along the Z-axis for application in medical imaging and increasing out-of plane resolution of 3-D medical image sets. Interpolation along the Z-axis is an essential task in clinical studies for better diagnosis and analysis of body organs and their functions. It is also necessary when sets of images with different out-of plane resolutions should be analyzed together.

The first part of the thesis discusses a 3-D interpolation method based on a piece-wise autoregressive model that has been already proven to be efficient for 2-D image interpolation.The 3-D image set is modeled as a 3-D piece-wise autoregressive model and the model parameters are estimated within a cube that slides through the low resolution image set.

The major part of this thesis is devoted to a new interpolation algorithm, called context-based 3-D interpolation. The proposed method represents a new approach of aiding 3-D interpolation and improving its performance by efficient use of domain knowledge about the anatomy, orientation and imaging modalities. In the new approach a family of adaptive 3-D interpolation filters are designed and conditioned on different spatial contexts (classes of feature vectors). Training is used to incorporate the domain knowledge into the design of these interpolators. Experimental results show significant improvement of the new approach over some existing 3D interpolation techniques.

Acknowledgements

I would like to express my sincere gratitude to my supervisors, Dr. Shahram Shirani and Dr. Xiaolin Wu for their immeasurable amount of support, guidance and encouragement through out my graduate studies at McMaster University.

Many thanks to Dr. Michael D. Noseworthy for providing medical image sets, Dr. David H. Frakes from Arizona State University for algorithms comparison and my committee members Dr. Aleksandar Jeremic and Dr. Thomas E. Doyle.

My deepest gratitude goes to my family for their unconditional love and giving me the opportunity to follow my dreams.

I would also like to acknowledge all of my friends for bringing a lot more fun and happiness to my life here at Hamilton .

Notation and abbreviations

CT Computer Tomography

SPECT Single Photon Emission Computed Tomography

MRI Magnetic Resonance Imaging

MIP Maximum Intensity Projection

SAI Soft decision estimation for Adaptive image Interpolation

CGI Control Grid Interpolation

MCGI Modified Control Grid Interpolation

CBI Context Based Interpolation

HR High Resolution

LR Low Resolution

PAR Piece-wise Autoregressive

CALIC Context Adaptive Lossless Image Coder

PSNR Peak Signal to Noise Ratio

RM Relevance Measure

ST Smoothness Threshold

Contents

List of Figures

Chapter 1

Introduction and Problem Statement

Medical imaging is the technique and process employed to create images of human body for clinical purposes. It is a necessary part of radiological sciences for visualization of anatomical structures and analysis of metabolic functions. Besides providing valuable information resources about human anatomy, functions of organs and related physiological processes, structural and functional imaging allow for analyzing the physiological behavior of an organ or tissue under treatment. In the past three decades medical imaging technology has experienced significant improvement. Creation of multi-dimensional imaging modalities is direct result of such advancements. The capability of multi-dimensional imaging modalities in attaining anatomical, physiological, metabolic and functional data from human body makes them very useful in radiological diagnosis. While in planar imaging some diagnostic features may be missed, the visualization of multi-dimensional images have assisted in discovering hidden features and providing significant clinical information for diagnosis and treatment. In broad sense medical imaging modalities are classified into two categories. According to their category they could provide details about either anatomical structures or functional activities. The former uses external source of energy as a mean to get information about the organ being imaged while the latter uses internal energy source (e.g. radioactive pharmaceutical injected to body) for the same purpose. X-ray Computed Tomography (X-ray CT) and Single Photon Emission Computed Tomography (SPECT) are examples of modalities obtained by external and internal energy sources, respectively. Besides, some modalities such as Magnetic Resonance Imaging (MRI) use both external and internal source of energy radiation. For a better clarification, classification of imaging modalities based on the applied energy source is illustrated in Fig. 1.1.

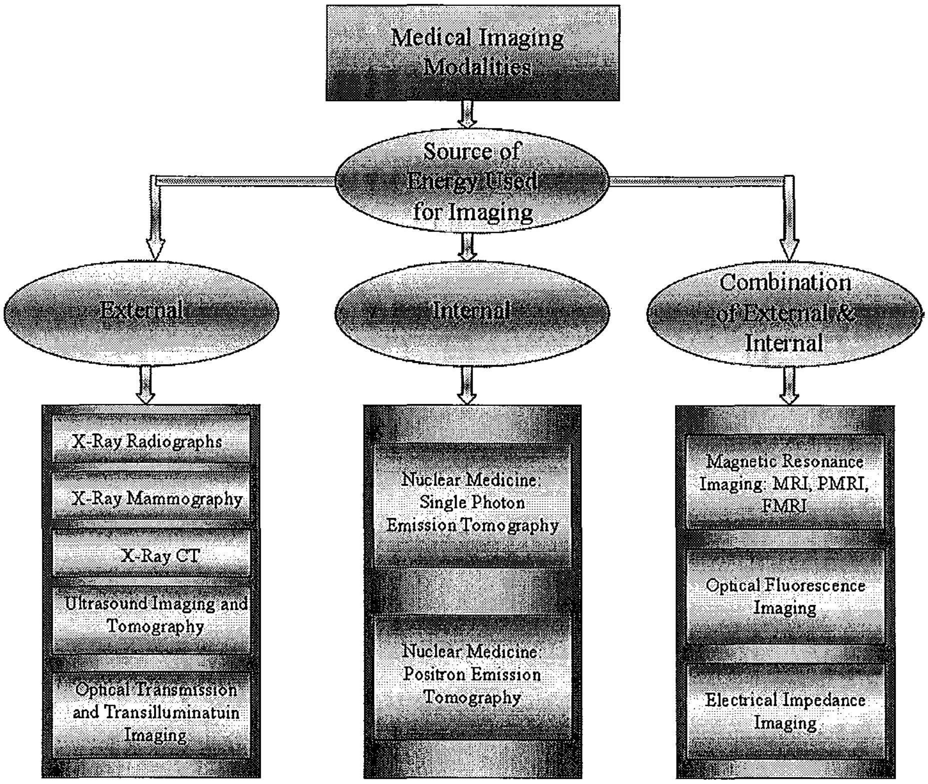

Figure 1.1: Different imaging modalities based on energy source used for imaging [1]

Upon radiation, the energy interacts with the specific body organ and the resulting signal, altered radiated energy, is collected and converted to a digital image by an image processing module called data (image) acquisition unit. A simple schematic of a medical imaging system is shown in Fig. 1.2. The accuracy, sensitivity and specificity factors of medical images may change due to limitation of different imaging modalities. Image processing techniques prove to have a critical role in improving the visibility and quantification of features of interest.

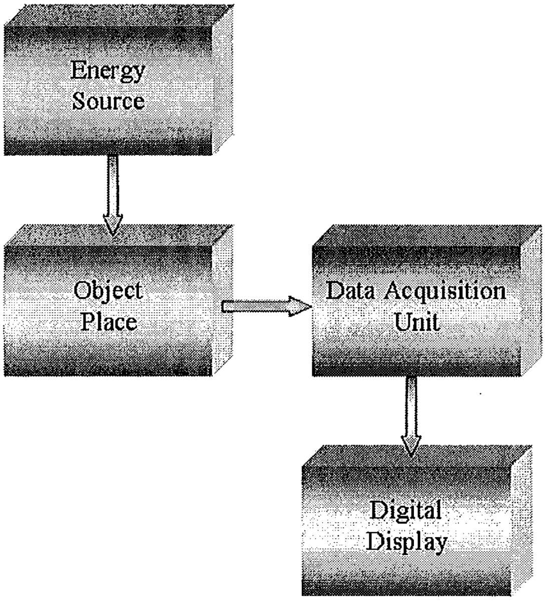

Figure 1.2: General schematic of a medical imaging system

One of the popular and common practice in clinical diagnosis is manipulation and analysis of 3-dimensional image modalities. A practical image analysis method frequently used in medical applications is visualization. It is an efficient mean of determining functions of internal organs and detecting possible causes of their malfunctions. With the ability to visualize important structures in great details, 3-D visualization methods are a valuable resource for the diagnosis and surgical treatment of many pathologies. For example Maximum Intensity Projection (MIP), a computer visualization method, is used for the detection of lung nodules in lung cancer. MIP intensifies the 3-D structure of the nodules, making them stand out from pulmonary bronchi and vasculature.

Medical imaging devices often produce set of 2-D images known as slice which forms a 3-D volume. Different method of scanning will result in different resolution within the image plane or along Z-axis (between slice resolution). For example a faster scan results in lower resolution along Z-axis and in most cases the sampling rate within the image plane (slice) is much higher than between them. As a result, voxels (volumetric pixels) are anisotropic (non-cubical) in the 3D space. An image set with higher 3-D resolution requires either more radiation exposure (such as in CT) or increased scan time (such as in MRI) which is impossible in many practical situations. However isotropically (or at least near isotropically) sampled data is a definite requirement for effective analysis and interpretation of medical images. Visualization of a non-isotropic volume will result in an incorrect aspect ratio that may cause geometric distortion and unequal magnification. It ultimately could bias the analysis and diagnosis process. For a more clear justification over the difficulty when visualizing a non-cubic image set, we encourage the reader to take a moment examining Fig. 1.3. In the figures a horizontal cross section is created first using a non-cubical set ($512 \times 512 \times 212$) and then using another set which is near-cubical ($512 \times 512 \times 420$).

To overcome the shortcoming of non-cubical voxles and make the sample distance same in x, y and z directions, a number of 3-D interpolation methods have been published. The proposed interpolation methods are based on different mathematical and physical concepts but what they all share in common is estimation of the intermediate unknown slice from statistics or geometrical features available in neighboring slices. It is worth mentioning that the application of 3-D interpolation is not necessarily confined to the problem of non-isotropic volumes but other cases such as changing the coordinate system or grid orientation may as well require interpolation. Another example of application of 3-D interpolation

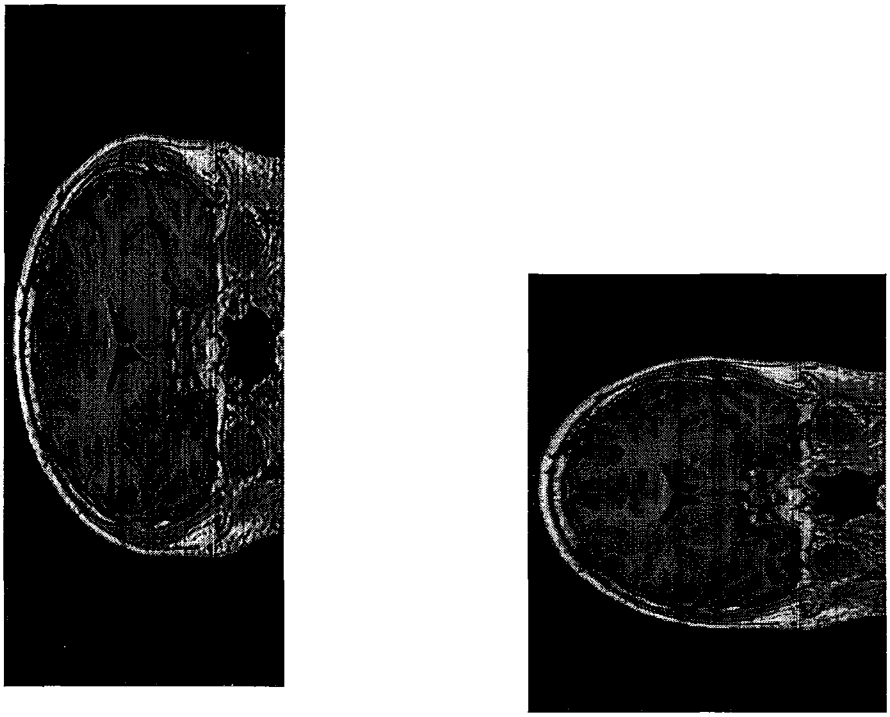

a. Non-Cubical Image Set: 512 × 512 × 212 b. Near Cubical Image Set: 512 × 512 × 420

Figure 1.3: Creating horizontal cross sections from non-cubical and near cubical image sets

is resolution assimilation which is indispensable when two image sets (either from same or different modalities) with different resolutions along Z-axis are to be analyzed simultaneously. In this situation interpolation will balance the resolutions and allow for more accurate analysis.

By now, the importance of 3-D interpolation is clearly manifested. It is also evident that the improvement of medical scanners' rate would not eliminate the need for interpolation. In the coming section a number of 3-D interpolation methods for medical images are reviewed.

1.1 Literature Review

The issue of interpolation for 3-D medical images became subject of interest following the need to display and visualize 3-D medical image modalities. In late 1970's modern tomography devices began to capture images of body organ in a slice-by-slice fashion. The first commercially viable CT scanner was publicly announced in 1972 and the first MR image was published in 1973. It was in 1977 when MRI was used to perform study on human. Digital geometry processing, applied on series of 2-D images, pioneered visualization of 3-D images of organs inside human body. As already discussed, visualization often requires an isotropic image set. It was since then that many 3-D interpolation techniques were proposed to resolve the problematic issue of anisotropic sets.

3-D interpolation techniques are generally classified into two classes: object-independent (non-adaptive to local statistics) and object-dependent (adaptive to local statistics). In the literature of 3-D medical image interpolation these two classes are referred to as scene-based and object-based, respectively. Though this classification was mentioned implicitly in early 80's [2] it was no sooner than late 90's when it was explicitly stated as scene-based and object-based [3]. Scene-based interpolation techniques exploit basis functions and kernels [4, 5] to estimate voxel value of an unknown slice from neighboring slices. The unknown voxel is usually calculated by weighted summation of voxel intensity values in two or four neighboring slices. The weighted values depend on the specific selected kernel. These methods are fast and low in computational complexity, however they result in significant artifacts when the edges shift considerably from one slice to another. Nearest neighbor, linear, cubic spline, modified cubic spline [6], cubic convolution [7], sinc-based and Kriging [8] are some examples of scene-based interpolation class. On the other hand, object-based interpolation methods explore the features within the slices to impose a more effective interpolation process considering edges and feature locations. The object-based methods have shown superior performance compared to scene-based algorithms but at the cost of more computational complexity. Thus choosing the suitable interpolation method is often a trade-off between computational complexity and accuracy. Object-based methods can be divided into two major groups: registration-based and shape-based method. The former has also been addressed as slice matching or correspondence [9]. The registration-based methods try to find an optimal transformation to map extracted contours and surface boundaries of a segmented slice to contour of a neighboring slice. Method of finding the map function is what makes for different registration-based interpolation techniques. For example Goshtasby et al. in [9] used feature points from consecutive slices based on gradient value and voxel intensity. (There are also different algorithms for contour extraction and conversion to geometrical shapes discussed in [10, 11] but they are not focus of this work.) Upon registering the contours, the intensity value of the contour in the unknown intermediate slice is calculated usually through linear interpolation. The other object-based method, shape-based interpolation utilizes the concept of distance transform. Depending on the choice of distance transform function, different methods of shape-based interpolation have been proposed such as in [12, 13]. Here we review and compare different algorithms proposed during the past three decades.

As we mentioned earlier the most convenient method of interpolation is to estimate the voxel intensity of the unknown slice by linearly combining the voxel intensity of the two neighboring slices such as in work of Liang et al. [14], Fuchs et al. [15] or Herman and Coin in [16]. Keys in [7] used higher order functions (cubic convolution) to estimate a more accurate waveform to fit the statistics within the slices. However the spacing of slices along Z-axis in medical images is not small enough to help a higher order function fit a better waveform to local statistics; thus a higher order interpolator or other scene-based interpolators would not work better than a linear interpolator [17]. The linear interpolator or any other interpolator of scene-based class perform poorly in case of considerable shift of edges (which happens specially when between slice spacing is more than $4mm$) or branching which is a common issue in medical images (e.g. imaging of coronary arteries). As to reduce the artifacts incurred in scene-based interpolation Lin et al. in [12] proposed a method based on concept of contour registration. Their method, elastic surface interpolation, attempted to solve the branching problem by determining a force field. This force field acted to distort an extracted contour in one slice to look close to the corresponding contour in another slice. Besides the computational complexity, the geometrical criteria introduced in Lin et al. algorithm failed to handle highly dissimilar contours and the results suffered from unwanted artifacts. Chen and Lin in [13] introduced surface consistency theorem and combined it with elastic interpolation and spline theory to settle the issue of contours dissimilarity. This method performed better in case of sever branching and dissimilar contours at the expense of more time and computation. Later, Raya and Udupa in [18] developed a simpler and more efficient scheme called shape-based interpolation. This method consisted of sequences of image segmentation and conversion of binary values to gray-level values followed by interpolation between known values. Distance transform was exploited for conversion from binary value to gray level value. The resulted gray value represented the distance of a voxel to a specific contour; in other words, instead of intensity interpolation, the distance was interpolated and this served geometric changes better. Generally speaking, the distance transform function estimates the shortest Euclidian distance between the voxel and the contour. (The reader may refer to [19] and [20] to get more information about distance transform functions.) Some other modified shape-based interpolation methods were published based on the same idea but using different distance transform functions such as in [21, 22]. Shape-based interpolation then became a popular choice of interpolation as it was efficient to implement and attained descent interpolation results. However this class of methods performed less desirable in the situation where alignment was necessary; specifically it could not handle objects with no overlap in consecutive slices, objects with holes and invagination. We should also mention that distance transform is a time consuming operation, specially in higher dimension. The method proposed by Guo et al. in [23], morphology-based interpolation aimed to overcome the problem of non-overlapping objects. In this method non-overlapping regions were interpolated through sequence of dilation and erosion operations. The reader may refer to [24] for more explanation on the mentioned operators. Another morphology-based interpolation method was developed by Lee and Wang in [25] which was more efficient in terms of computational complexity. Chatsiz and Pitas method in [26] which relied on mathematical morphological skeletonisation for object representation is also another example of this class. The morphology-based methods can effectively deal with objects with whole and invagination, yet it fails in resolving the problem in massively invaginated objects [27]. Another fact to consider is that shape-based and morphology-based algorithms can not be applied to gray-level images [28]. Grevera and Udupa in [29] modified the shape-based interpolation algorithm with two additional steps of lifting and clasping to make it applicable to gray level images as well.

In the past decade more efficient methods have been formulated using more advanced registration methods to effectively balance the trade-off between speed and visual quality. Lee and Lin in [30] applied the concept of image-warping of [31] to their interpolation method to achieve a faster algorithm and computed line-segments automatically. Registration-based method published by Penny et. al in [28] utilized a more modern and effective registration method called voxel-based nonrigid registration. The mentioned registration method was first introduced by Rueckert et.al in [32]. In 2008 Frakes et al. in [33] developed an object-based method of interpolation based on an improved version of control grid interpolation (CGI). CGI is a common motion compensation method combining block-matching and optical flow. For further reading about CGI the reader may refer to [34]. This optical flow based method in Frakes et al. work is called modified control grid interpolation (MCGI). They modified conventional CGI by incorporating adaptive optimization, putting a constraint on displacement field precision and adding more displacement fields. As opposed to Penny et. al method, MCGI is directionally unbiased. To the knowledge of the author, it has been the most competent interpolation algorithm both in terms of computational efficiency and visual quality.

1.2 Thesis Contribution

In this work two 3-D adaptive interpolation methods are presented. The first method is an extension of SAI (Soft-decision Adaptive Interpolation) method in [35] to 3-D. A 3-D piece-wise autoregressive model is fitted to a 3-D block of slices and the model parameters are estimated through an optimization problem. The spacing between medical image slices differs significantly from pixel spacing of 2-D images; thus this method has limited performance for 3-D medical image interpolation. It is included as a part of the thesis because it fostered the second interpolation algorithm. The second method, context-based interpolation (CBI), is the main contribution of this thesis. CBI is a new 3-D interpolation method which is a supervised learning algorithm. A linear predictor of a gray value in a missing slice is trained. It takes into account, apart from gray values, some additional imaging attributes like modality, orientation and anatomy. In CBI, a large number of contexts are extracted form a training set. The contexts are classified based on the mentioned characteristics; then using classified contexts, linear interpolators are determined in the least square sense. When interpolating a slice, an optimal interpolator is selected based on the local statistics. The simulation results have proved that the proposed method outperforms existing methods for the chosen anatomy and modality.

1.3 Organization

The remainder of this thesis is organized as follows. Chapter 2 discusses the interpolation method based on a piece-wise autoregressive model. In chapter 3 the context-based interpolation method is presented. Finally in chapter 4 the concluding remarks and future works are discussed.

Chapter 2

Interpolation Based on an Auto Regressive Model

In this chapter, the proposed 3-D interpolation method is based on an auto regressive model and estimating group of voxles rather than estimating one voxel at a time. The idea was encouraged by a 2-D interpolation method called adaptive 2-D autoregressive modeling and soft-decision estimation (SAI) proposed by Zhang and Wu in [35]. They modeled an image as a piece-wise autoregressive process and estimated the parameters for this process based on local statistics of some samples within a window. In this work which is an extension of SAI to 3-D, the model parameters are estimated within a cube that slides through low resolution (LR) image set. The 3-D volume is modeled as a 3-D piece-wise autoregressive (PAR) process and the parameters to estimate high resolution (HR) slices are determined within a 3-D block of voxels.

2.1 3-D Piece-Wise Autoregressive Model

A 3-D volume can be modeled as a piece-wise autoregressive process as follows

$$I(i,j,k) = \sum_{(m,n,q)\in T} \alpha(m,n,q) I(i+m, j+n, k+q) + \varepsilon_(i,j,k) \tag{2.1}$$

where T is a 3-D template for the regression and $\varepsilon_(i,j,k)$ is the white noise, independent of the location. Such a model will adapt the model parameters, α's, to statistics of available voxels within the template. The model parameters are not supposed to vary significantly in a small locality. The PAR model has already been validated in lossless image compression such as CALIC [36], TMW [37] and invertible integer wavelet [38] (Besides, the validity of PAR model in 2-D image interpolation has been confirmed in SAI [35]).

2.2 Integration of PAR model into Adaptive 3-D Interpolation

Suppose that I_L is a slice in an LR set. I_L's are used to estimate the unknown slice I_h that belongs to the 3-D HR set. At the voxel level the unknown voxel $x_i \in I_h$ is to be estimated by $y_i \in I_L$. There are different choices of y_i's in a local cube that will be discussed later in simulation results section (see Fig. 2.2). Inspired by the PAR model, the missing voxel can be estimated as follows

$$x_i = \sum_{j=1}^{n} \alpha_j y_j + \varepsilon \tag{2.2}$$

where n is the number of known selected voxles. To estimate more than a voxel at a time, a local cube, W is defined that encapsulates a number of slices. Then the missing voxels are estimated within W

$$\hat{\mathrm{x}} = \arg\min_{x}\{\sum_{i\in W} \|x_i - \sum_{j=1}^{n} \alpha_j y_j\| + \sum_{i\in W} \|y_i - \sum_{j=1}^{n} \alpha_j x_j\|\} \tag{2.3}$$

The more accurate the model parameters, α's, are estimated, the more successful the interpolation algorithm would perform. These parameters are estimated using available slices in the LR set

$$\hat{\alpha} = \arg\min_{\alpha} \sum_{i\in W} (y_i - \sum_{j=1}^{n} \alpha_j y_j)^2 \tag{2.4}$$

Next we discuss the details of the algorithm.

2.3 Details of the Algorithm

In 3-D volumes, edges happen to shift considerably from one slice to another. To avoid possible artifacts, the neighboring 3-D blocks overlap. There are different choices of block size but let us consider the simplest case where 3 available slices are used to estimate 2 unknown slices (see Fig. 2.1). Equ. 2.3 is rewritten in a matrix format as follows

$$Min. \|BX - AY_1\| + \|Y_2 - CX\| \tag{2.5}$$

where B is a row vector containing either zero or one. The size of this vector is the same as the number of parameters. Depending whether a specific voxel in the local cube should be estimated or not, the elements of vector B are either one or zero accordingly. A is the vector of estimated parameters, Y_1 and Y_2 contain known voxels of known slices. C also contains model parameters but differs in size from A depending on how many voxels will be estimated in each interpolation pass. To solve the minimization problem of Equ. 2.5, F

is defined as follows

$$F = (BX - AY_1)(BX - AY_1)^T + (Y_2 - CX)(Y_2 - CX)^T \tag{2.6}$$

By taking derivative of 2.6 and setting it to zero, $\frac{\partial F}{\partial X} = 0$, the unknown voxels are determined as in 2.7

$$X = (B^T B + C^T C)^{-1}(B^T AY_1 + C^T Y_2) \tag{2.7}$$

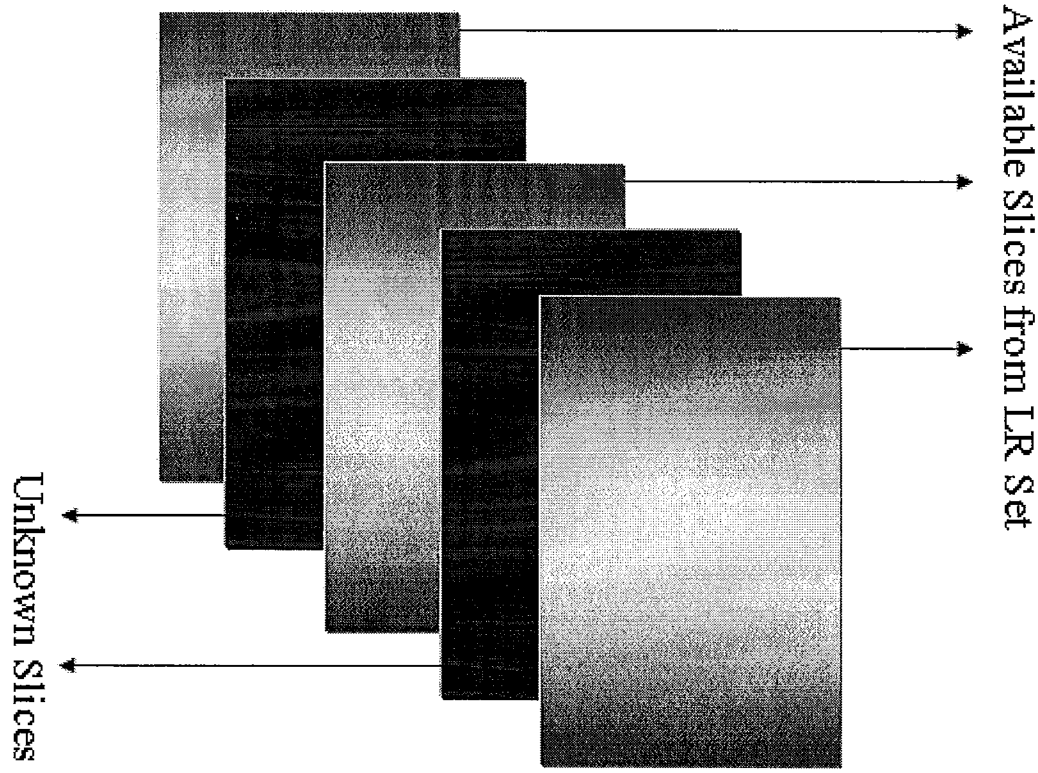

Figure 2.1: Position of known and unknown slices

2.4 Simulation Results

The simulation results prove the large spacing between medical image slices, violates the assumption that model parameters do not vary significantly in the selected locality. The minimum spacing between slices in an LR medical image set, used in this work, is $3.2mm$; this is significantly larger compared to pixel spacing in LR 2-D images. Parameter estimation, defined in 2.4, based on LR slices, leads in a less desirable results compared to linear interpolation. These results are regardless of overlap, selected voxels and the number of voxels estimated at a time. Different choices for the set of known neighboring voxels from available LR voxels are illustrated in Fig. 2.2. As the number of known voxels, engaged in estimation process, increases, interpolation results get better (e.g. in Fig. 2.2, configuration (e) works better than configuration (a)). Still at its best, the interpolation results are few (dB) below the linear method (see Fig. 2.3). Then, to improve the results, linear approximation of the missing HR slices is used to estimate model parameters. This time the interpolation results are almost the same as linear interpolation (see Fig. 2.4). The PSNR values, obtained using PAR-based interpolation, versus the linear interpolation for some brain MRI images have been plotted in Figs. 2.3 and 2.4. In Fig. 2.3, LR slices are used to estimate model parameters and in Fig. 2.4 the linear estimate of unknown slices are employed for the same task. In both cases 9 voxels from each neighboring slices are chosen and the 3-D block consists of 3 LR slices.

2.5 Conclusion

The large spacing between slices in an LR medical image set, frustrates the accurate model parameter estimation. Evaluating the model parameters using linear approximation of HR set produces results similar to linear interpolation. This gives the impression that the model parameters are estimated to be as similar as possible to linear interpolator parameters; thus a better estimation of unknown HR slices, results in more accurate interpolation. This is verified using real HR slices as the primary guess for unknown slices. In this case the algorithm produces slices almost the same as the real HR slices. But in real application there is no access to HR slices. This observation inspired the idea of employing a training set to learn about an HR image set, then applying the obtained knowledge when the HR set is not available. The next chapter discusses interpolation based on training.

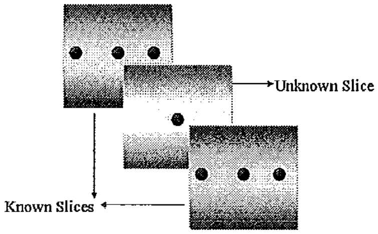

a. 3 voxels from each available neighbor of unknown slice

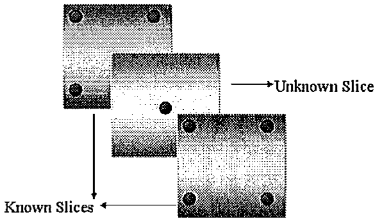

b. 4 voxels from each available neighbor of unknown slice

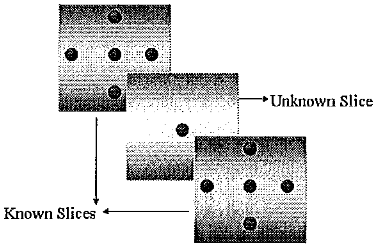

c. 5 voxels from each available neighbor of unknown slice

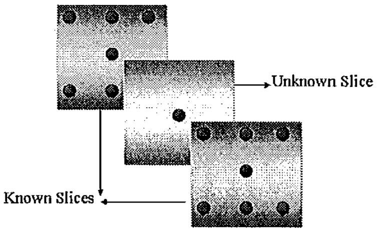

d. 7 voxels from each available neighbor of unknown slice

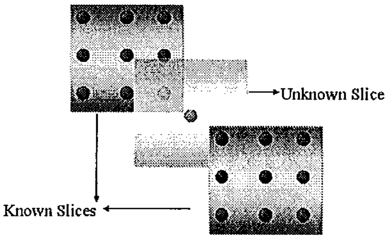

e. 9 voxels from each available neighbor of unknown slice

Figure 2.2: The different choices for selection of voxels from available neighbors of an unknown slice

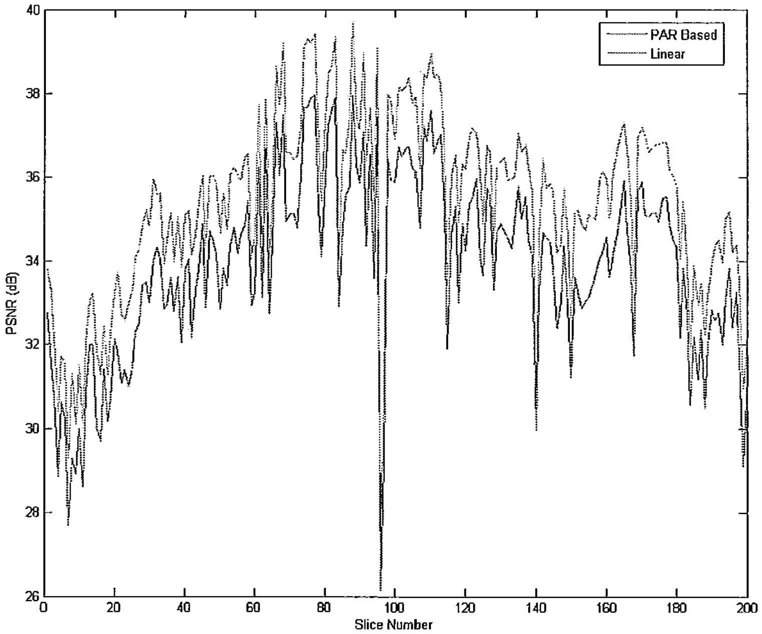

Figure 2.3: PSNR values, PAR-based vs. linear, using slices in LR set to determine model parameters

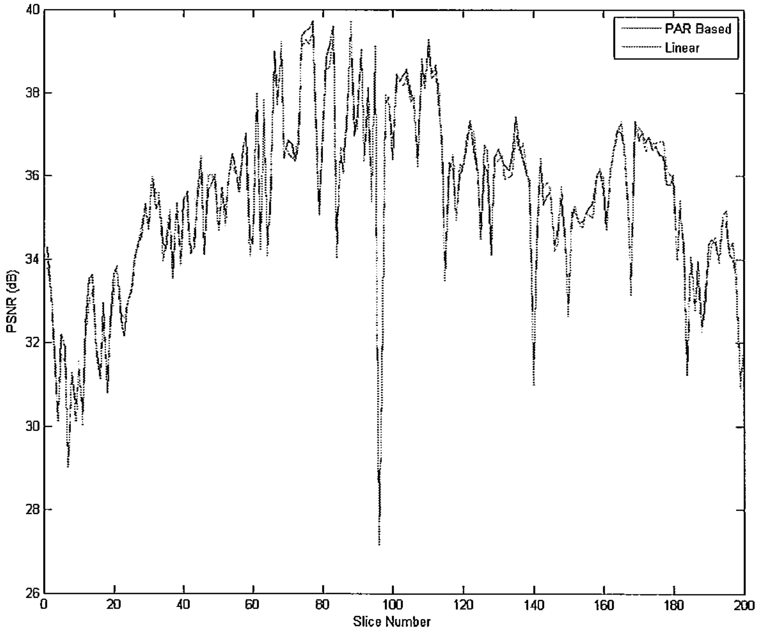

Figure 2.4: PSNR values, PAR-based vs. linear, using linear estimate of missing HR slices to determine model parameters

Chapter 3

Context-Based Interpolation

3.1 Overview

Recently a few 2-D image interpolation algorithms have been proposed based on concepts of machine learning and utilization of a training set of HR images such as in [39, 40]. A training set is able to provide knowledge that is unavailable in an LR image set. Interpolation based on learning consists of two related processes: off-line training to learn about an HR set, and an online adaptive interpolation. By down sampling the HR image sets in a training set, we would create the corresponding LR set and predict the statistical relationship between HR and LR set. The purpose of off-line training is to learn the rules for estimation of an unknown HR slice from available LR set of slices. As structure of samples in any image set, including medical image sets, is non-stationary, it is impossible to govern a general rule for all the existing cases. Thus the sample statistics observed in the training are used to determine the necessary context-based rules that adapt an interpolator to the local 3-D waveforms. These context-based interpolators can run in real time when applied online because the interpolation is performed by simple context quantization (i.e., feature vector classification) followed by linear filtering.

In this chapter we describe the off-line design process of context-based 3-D interpolators, and develop required algorithms. Then we present the online procedure of applying the proposed context-based 3-D interpolation technique. Experimental results are then reported and then comes conclusion section.

3.2 Context-based 3-D Interpolator Design

Instead of using linear signal-independent 3-D interpolators, we propose a family of context-based adaptive 3-D interpolators. Such an interpolator uses four existing slices to interpolate the missing slice in the middle as depicted in Fig. 3.1. As shown in the figure the interpolator is an M-tap 3-D filter that estimates the missing voxel x using the M neighbors $\mathrm{y} = (y_1, y_2, \cdots, y_M)$ of x ($M = 20$ in Fig. 3.1). In the language of pattern recognition and machine learning the vector y is called the context or feature vector of x. The interpolated value of x is given by

$$\hat{x} = \sum_{1 \le m \le M} \mathrm{a}_m y_m, \tag{3.1}$$

where a_m's are the interpolator coefficients. The interpolator can be optimized in least squares sense using a large training set of feature vectors y_t and the associated center voxels x_t. Specifically, the optimal interpolator a_* is given by

$$\mathrm{a}_* = \arg\min_{\mathrm{a}} \sum_t (x_t - \mathrm{a} \cdot \mathrm{y}_t)^2. \tag{3.2}$$

However, the above design approach is over simplistic because typical 3-D medical images are highly non-stationary in space. Different localities of a 3-D image may have

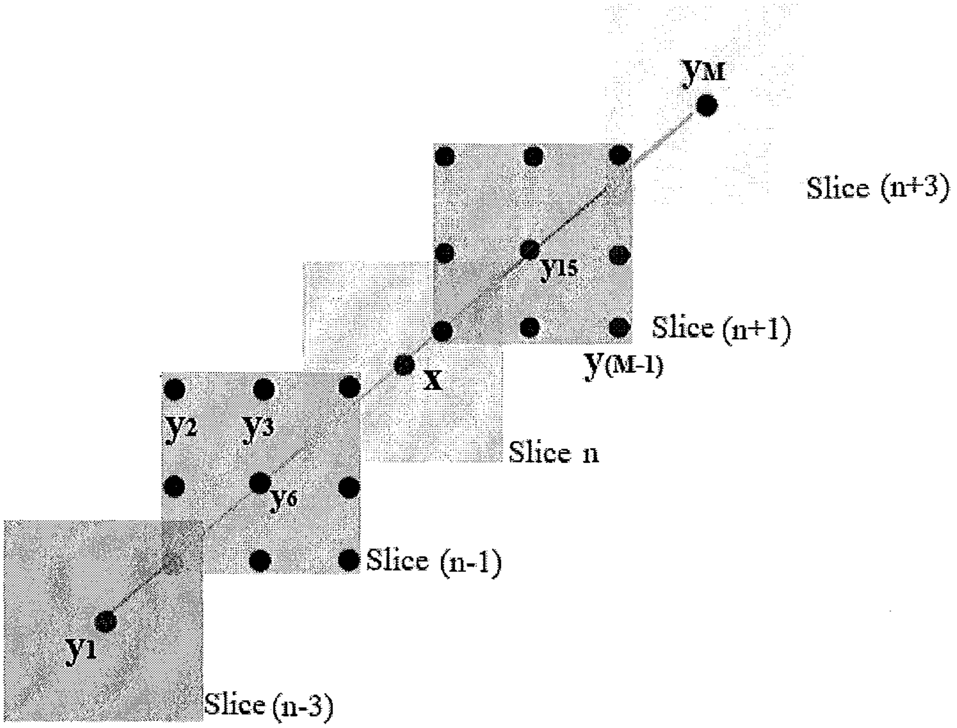

Figure 3.1: A missing voxel x in the context $\mathbf{y}$

drastically different second-order statistics. It is impossible to design a single interpolator $\mathbf{a}_*$ to fit all 3-D waveforms of a medical image set. A large number of contexts is the preliminary requirement to distinguish different waveforms. Supposing the context consists of M number of LR voxles of L gray level, there could be up to L^M possible context combination. The exponential complexity as well as data over fitting issue are factors that prohibit one from designing an interpolator for each individual context and no practical training set is capable of delivering enough sample to learn about all possible contexts.

For this reason, we quantize the feature vectors $\mathbf{y}$ into κ interpolation contexts ($\kappa <$

L^M), $Q(\mathrm{y}) = \{1, 2, \cdots, \kappa\}$, and design a least-squares interpolator for each context:

$$\mathrm{a}_k = \arg\min_{\mathbf{a}} \sum_{Q(\mathrm{y})=k} (x - \mathrm{a} \cdot \mathrm{y})^2, \ \ 1 \leq k \leq \kappa \tag{3.3}$$

The context quantization of y can be performed by any vector quantizer. For instance, we can adopt the classical k-means algorithm. But in medical image applications, users typically know many properties of the image, such as anatomy, imaging modality, projection orientation, age and gender of the patient, etc. Therefore, one can classify 3-D medical images into classes according to the aforementioned or similar attributes, and optimize the 3-D interpolator for each class. This classification approach can improve interpolation performance because it reduces the statistical variations. The classification can be further refined to the object level. For instance, for an MR 3-D head sequence of N slices I_1, I_2, ..., I_N, we can sequentially partition the N slices into J group of slices: $S_j = (I_{q_{j-1}}, \cdots, I_{q_j})$, $1 \leq j \leq J$. Each group, S_j, consists of nearby slices of similar statistics. The merits of this slice grouping can be clearly seen in Fig. 3.2. In this case, when the 3-D volume is traversed top down slice by slice, there are significant changes in object structures and intensity distribution. On the other hand, the statistics remain fairly consistent within a group of consecutive slices (see Fig. 3.4). Obviously, a 3-D interpolator optimized for a group of slices will be more accurate than the one designed using statistics of all the N slices. In the next section we discuss developing an optimal slice grouping algorithm.

3.2.1 Optimal J-Grouping of the Training set

We develop an optimal J-grouping algorithm to group slices of the training set based on similarity of the slices in a group of slices. The similarity measure used is the mutual

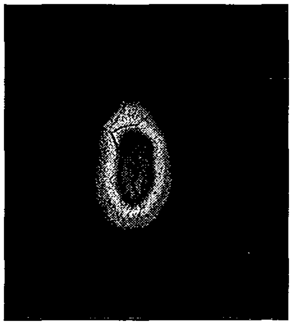

Slice No.12

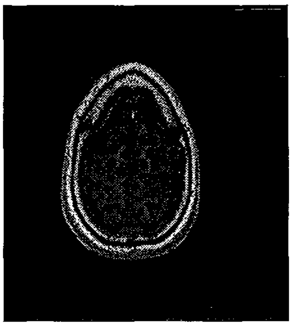

Slice No.32

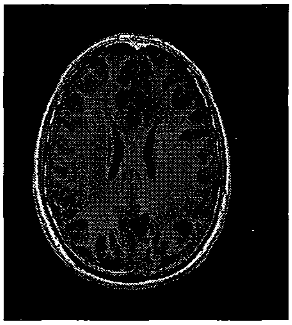

Slice No.79

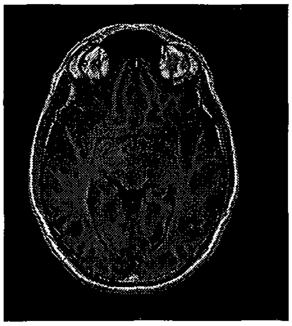

Slice No.117

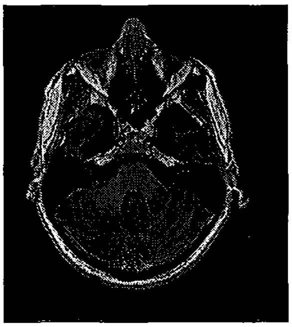

Slice No.154

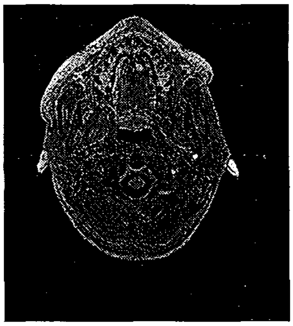

Slice No.207

Figure 3.2: Different anatomy in slices according to their number

information. Under the criterion of maximizing the mutual information per group of slices, we partiton slices in different groups. The mutual information of two random variable Φ and Θ is defined by

$$MI(\Phi, \Theta) = \sum_{\phi \in \Phi} \sum_{\theta \in \Theta} p(\phi, \theta) \log \frac{p(\phi, \theta)}{p_1(\phi) p_2(\theta)} \tag{3.4}$$

where $p(\phi, \theta)$ is the joint probability density function of Φ and Θ, and $p_1(\phi)$ and $p_2(\theta)$ are the marginal probability density functions of Φ and Θ respectively.

The J grouping is defined by the vector or quantizer $\mathrm{q} = (q_0, q_1, \cdots, q_J)$. The task is to find the number of groups, J, and the location of partitioning positions $1 = q_0 < q_2 < \cdots < q_{J-1} < q_J = N$ such that the sum of mutual information between slices within a group would be maximized.

$$\mathrm{q}_j = \arg \max_{\mathrm{q}} \sum_{j=1}^{J} \sum_{i=q_{j-1}}^{q_j} MI(I_i, \hat{I}_j) \tag{3.5}$$

where $\hat{I}_j$ is a representative chosen for a group. There are different approaches for assigning the representative, for example choosing the middle slice in the interval. Then the number of slices in group S_j is

$$N_j = \mathrm{q}_j - \mathrm{q}_{j-1} + 1 \tag{3.6}$$

The above formulation will just yield the number of slices within each group and the number of groups should be known beforehand. As the purpose is to find both number of groups and slices within each group, a heuristic method is developed. It simultaneously determines both partitioning positions and number of slices within each group as follows

Step1. We define $A = MI(I_1, I_{\lfloor \frac{N}{2} \rfloor})$, $B = MI(I_{\lfloor \frac{N}{2} \rfloor}, I_N)$ and $d = A - B$ where

$\lfloor \frac{N}{2} \rfloor$ is the largest integer not greater than $\frac{N}{2}$. If $A > B$ then $I_{\lfloor \frac{N}{2} \rfloor}$ belongs to the first group and $\lfloor \frac{N}{2} \rfloor$ is updated to $\lfloor \frac{N}{2} \rfloor = \lfloor \frac{N}{2} \rfloor + 1$; otherwise $I_{\lfloor \frac{N}{2} \rfloor}$ belongs to the other group and $\lfloor \frac{N}{2} \rfloor$ is updated such that$\lfloor \frac{N}{2} \rfloor = \lfloor \frac{N}{2} \rfloor - 1$. We continue until parameter d changes sign. By then there are N_1 slices in the first group and N_2 slices in the second group. At this point two more parameters are defined as follows $MI_1 = \frac{1}{N_1} \sum_{i=1}^{N_1-1} MI(I_i, I_{i+1})$ and $MI_2 = \frac{1}{N_2} \sum_{i=1}^{N_2-1} MI(I_i, I_{i+1})$.

Step2. The same procedures as in step 1 are followed for the newly obtained groups. The normalized total sum of mutual information for each new group is compared with the same value from the higher level. When the difference between current value and the former value is smaller than a defined threshold μ, the algorithm stops.

This process is better described in the flow chart of Fig. 3.3.

For each group, S_j, a representative I_{j^*} is selected based on the following criterion

$$j^* = \arg \max_{q_{j-1} \leq r \leq q_j} \sum_{q_{j-1} \leq i \leq q_j} MI(I_i, I_r) \tag{3.7}$$

This representative will later used in online process to determine the relevant group an input slice belongs to.

Partitioning the training set into J groups reduces the statistical variations within each group. In order to make the statistics in the design of context-based interpolators even more consistent, we further quantize the samples of each group S_j, $1 \leq j \leq J$, into K states $C_{j,k}$, $1 \leq k \leq K$.

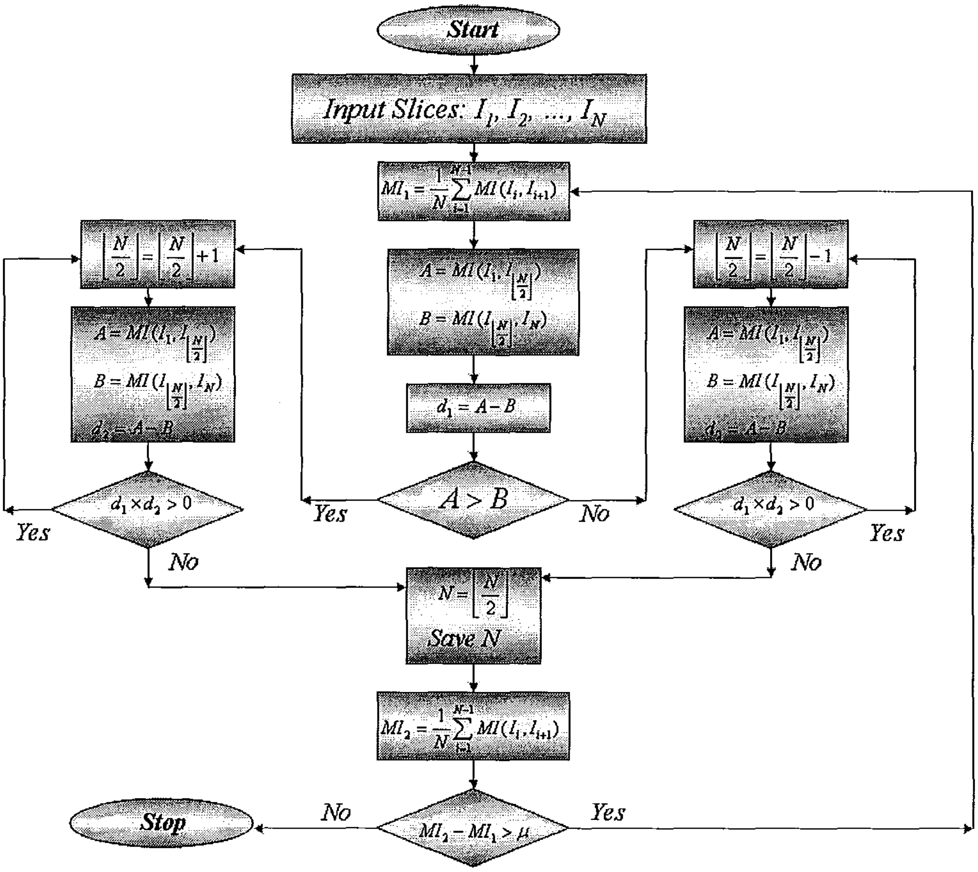

Figure 3.3: Optimal J-grouping algorithm

3.2.2 Optimal Design of Interpolator for each Group

Each of the groups is considered as a distinct training set. For any voxel $\mathbf{x}$, its associated feature vector (see Fig. 3.1) is extracted and stored. When all voxels and their corresponding feature vectors are stored, a clustering algorithm will further quantize the samples. We used k-means algorithms for the clustering purpose. The k-means algorithm is locally optimal and the final clustering depends heavily on the initial choice of states, $C_{j,k}^{(0)}$,

Slice No.32 Slice No.33

Slice No.34 Slice No.35

Figure 3.4: Similarity of anatomy in consecutive slices

$1 \leq k \leq K$. We initialized k-means by utilizing quantized interpolation error of a non-adaptive interpolator. For each center voxel x and its feature vector y, the bicubic interpolation error, $e_i = \mathrm{x}_i - G.y_g$, is calculated; where G is bicubic interpolator coefficients and $y_g = (y_1, y_6, y_{15}, y_M)$ (see Fig. 3.1). A uniform quantizer is then used to quantize the error. Thus the initialization is as follows

$$(\mathrm{x}_i, \mathrm{y}_i) \in C^0_{j,k} \ \ if \ \ Q(e_i) = k \tag{3.8}$$

This two-layer feature vector quantizer is depicted in Fig. 3.5. By conditioning on the state $C_{j,k}$ of feature vectors, a more accurate interpolator can be designed whose coefficients are denoted by $\mathrm{a}_{j,k}$. Specifically, the interpolator coefficients $\mathrm{a}_{j,k}$ are computed by

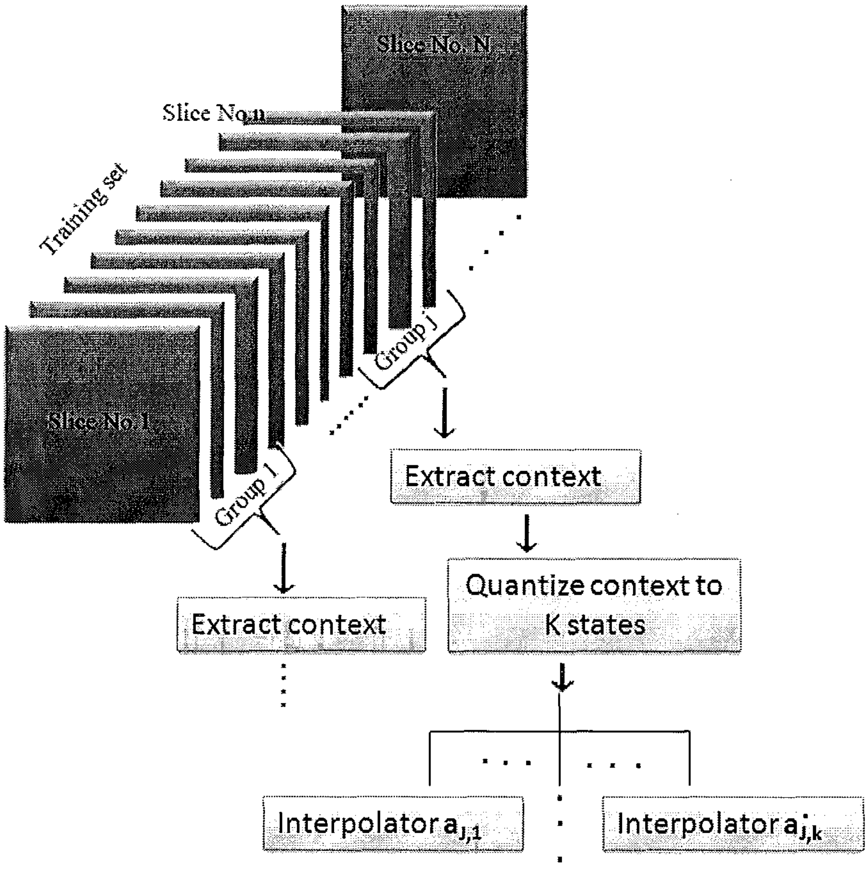

Figure 3.5: Off-line process for designing the interpolator

(3.3).

3.3 Online Interpolation Process

For the context-based interpolator, designed for $C_{j,k}$, the corresponding M-tap linear filter (in our case $M = 20$) $\mathrm{a}_{j,k}$ and the centroid $\bar{\mathrm{y}}_{j,k}$ of the $C_{j,k}$ are stored. To interpolate a missing voxel x in the context y, we first determine the state that y belongs to. Suppose that x is in between two LR slices I_i and I_{i+1}. The average of inputs is defined as $I_{ave,i} =$

$\frac{1}{2}(I_i + I_{i+1})$. The best match for the primary classification layer (group of slices) is searched out as follows

$$I_{ave,i} \in S_{j^*} \;\; if \;\; \|I_{ave,i} - I_{j^*}\|_2^2 < \|I_{ave,i} - I_j\|_2^2, 1 \leq j, j^* \leq J \tag{3.9}$$

where I_{j^*} and I_j are representatives of groups. Then we find the state k_j^{**} in the group j^* by nearest neighbor search, namely,

$$k_j^{**} = \arg \min_{1 \leq k \leq K} \|\mathrm{y} - \bar{\mathrm{y}}_{j,k}\|_2 \tag{3.10}$$

and we use the interpolator $\mathrm{a}_{j,k_j^{**}}$ to estimate the missing voxel x to be

$$\hat{x} = \mathrm{a}_{j,k_j^{**}} \cdot \mathrm{y} \tag{3.11}$$

However some slices may happen to be near the borders of two groups. In such cases combination of knowledge from both groups results in a better voxel estimation. Suppose the contexts belong to S_{j^*}. We define $E = \|I_{ave,i} - I_{j^*}\|_2^2$, $E1 = \|I_{ave,i} - I_{j^*+1}\|_2^2$ and $E2 = \|I_{ave,i} - I_{j^*-1}\|_2^2$. If either $|E - E1|$ or $|E - E2|$ is smaller than a predetermined threshold, the missing slice is considered as a border slice. In this situation we compute k_j^{**} and k_{j+1}^{**} (k_{j-1}^{**}) and estimate x as

$$\hat{x} = \frac{e_{j+1}^2}{e_j^2 + e_{j+1}^2} \mathrm{a}_{j,k_j^{**}} \cdot \mathrm{y} + \frac{e_j^2}{e_j^2 + e_{j+1}^2} \mathrm{a}_{j,k_{j+1}^{**}} \cdot \mathrm{y} \tag{3.12}$$

where $e_j^2 = \|\mathrm{y} - \bar{\mathrm{y}}_{j,k_j^{**}}\|_2^2$ and $e_{j+1}^2 = \|\mathrm{y} - \bar{\mathrm{y}}_{j,k_{j+1}^{**}}\|_2^2$. In other words, we fuse, in least-squares criterion, the results of the two context-based interpolators whose coefficients are $\mathrm{a}_{j,k_j^{**}}$ and $\mathrm{a}_{j,k_{j+1}^{**}}$ ($\mathrm{a}_{j,k_{j-1}^{**}}$), respectively. This is a safeguard against statistical mismatches between input slices and the training set. A summary of interpolation process is illustrated in Fig. 3.6

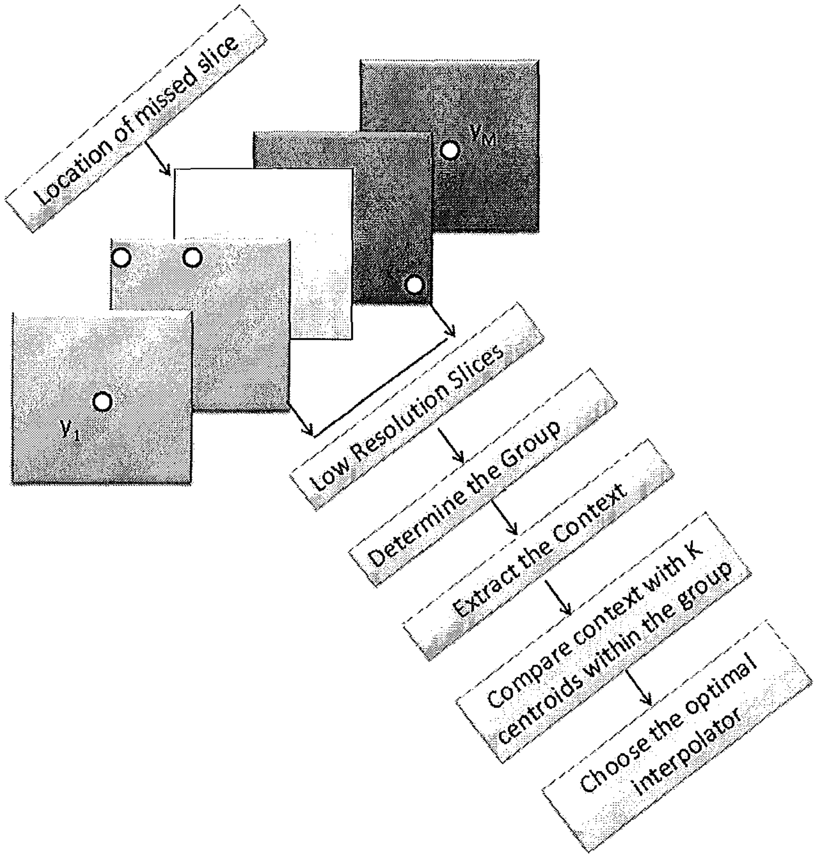

Figure 3.6: Interpolation Process

3.3.1 Algorithm Speed-Up

Depending on the location of a missing voxel and the neighborhood statistics, linear interpolation may or may not perform well. Locating the areas where linear interpolator can perform satisfactory will decrease the computation time. We have introduced two smoothness measures and depending on their magnitude decide about the suitable interpolator.

3.3.1.1 Second-Order Derivative

We used 3-D discrete Laplace operator to measure the smoothness. Laplacian is determined in X, Y and Z directions. The 1-D Laplacian estimation in a direction, e.g X, can be approximated as follows

$$D_X = \frac{I(X + 2h_X, Y, Z) - 2I(X + h_X, Y, Z) + I(X, Y, Z)}{h_X^2} \tag{3.13}$$

where h_X is grid spacing in X direction. Taking advantage of the property of multidimensional discrete Laplacians, the 3-D discrete Laplacian, L_{XYZ}, is computed by Kronecker sums of 1-D discrete Laplacians

$$L_{XYZ} = D_X \bigoplus D_Y \bigoplus D_Z \tag{3.14}$$

The smoothness measure, L_{XYZ}, is compared with a certain threshold as to make a decision about choosing either linear or context-based interpolator. Embedding this criterion into the interpolation algorithm keeps the visual and quantitative quality the same but would not decrease the algorithm run-time.

3.3.1.2 First-Order Derivative

The smoothness measure based on second order derivative did not save us computation time. So we considered another smoothness measure based on first order derivative as follows

$$D = |y_1 - y_6| + |y_6 - y_{15}| + |y_{15} - y_M| \tag{3.15}$$

where y_1, y_6, y_{15} and y_M are shown in Fig. 3.1. D, the smoothness measure, is compared with T, a smoothness threshold (ST). The choice of threshold is a trade-off between quality and computation time.

3.4 Simulation Results

We implemented the proposed context-based 3-D interpolation algorithm for medical images. The algorithm is tested on a number of 3-D sets of brain MRI to evaluate its performance. The trained context-based interpolators are applied to interpolate LR 3-D images that do not belong to the training set. The number of states $C_{j,k}$, for each group is different since the range of quantized error values varies for each group. The choice of step size for the uniform quantizer also results in different number of states. Decreasing the quantizer step size increases the run-time and improves the interpolation. However as the step size becomes smaller (i.e. < 3) the interpolation error does not improve significantly but the run-time increases drastically. In table 3.1 parameters of training set and test data are shown. MR images are acquired on a T_2 weighted scan sequence in a magnetic field of 3 Tesla. The orientation of images in the training set and the test data is the same and MRI samples of the training set belong to people in their 20's; however the author is unaware of the age range for the test images.

Table 3.1: Parameter of training set vs. test data for brain MRI

Data Class	Orientation	Ave No. of Slices	Slice Thickness (Spacing)	2-D Plane Size
Training Set	Axial	220	$1.6mm$	512×512
Test Sets	Axial	101	$3.2 - 4mm$	128×128 - 512×512

To show the superior performance of CBI, its performance is compared to two existing interpolation methods. The first interpolation method is the conventional linear interpolator and the other interpolator is MCGI introduced in [33]. MCGI is one of the latest and most competitive existing interpolation methods. The comparison criteria are based on PSNR and relevance measure (RM) values. PSNR is a common measure of comparison in most video/image processing tasks; however for medical image processing the relevance measure has been employed more frequently as in [33, 28]. The RM is defined as follows: Let MSD_1 and MSD_2 be the mean squared difference between the interpolated image and the original image for methods 1 and 2, respectively. Then the relevance measure of these two methods is

$$
\begin{aligned}
& r_{method1/method2} = \\
& +100 \times (1 - \frac{MSD_1}{MSD_2}) \quad if \quad MSD_1 > MSD_2 \\
& -100 \times (1 - \frac{MSD_2}{MSD_1}) \quad if \quad MSD_2 > MSD_1
\end{aligned}
\tag{3.16}
$$

In Fig. 3.7 the PSNR values of CBI versus the linear and MCGI interpolators is plotted for a sequence of brain images, with X-axis being the slice number. Then table 3.2 lists the relevance measures for CBI vs. the linear interpolator, MCGI vs. linear interpolator and CBI vs. MCGI. According to the relevance measures in table 3.2, the overall performance of CBI is superior to both MCGI and linear methods; CBI is also robust against changes in 2-D plane size. To demonstrate the difference between CBI and the other two methods in terms of visual quality, some interpolated sample images are presented in Fig. 3.9 to Fig. 3.14. The PSNR values of these samples are also given.

Table 3.2: Relevance measures for brain MRI

2-D Plane Size	$r_{mcgi/lin}$	$r_{cbi/lin}$	$r_{cbi/mcgi}$
512×512	24.13	34.17	13.23
256×256	31.4	37.54	8.93
128×128	39.63	42.38	4.56

Table 3.3: Trade-off between objective quality and computation time

$t_1 = 8$ *Sec for a* 512×512 *slice on a computer with 2.4GHz Intel CPU and 3.00 GB RAM in MATLAB 7.1*

Smoothness Threshold in Ascending Order	$r_{cbi/mcg}$	$r_{cbi/lin}$	Computation Time Percentage
No Threshold	13.23	34.17	t_1
T_1	14.47	35.2	$73\%t_1$
T_2	13.91	34.68	$71\%t_1$
T_3	13.35	34.26	$65\%t_1$
T_4	12.30	33.46	$57\%t_1$
T_5	11.24	32.66	$50\%t_1$
T_6	10.48	32.08	$45\%t_1$

Table 3.3 expresses the trade-offs between objective quality and the computation time as the smoothness threshold varies. A carefully selected smoothness threshold not only reduces the computation time but also improves the objective quality. The effect of increasing the threshold value in terms of visual quality has also been illustrated in Fig. 3.16 to Fig. 3.20.

CBI was also tested on series of abdominal MR images. The training set and test data parameters are shown in table 3.4. The PSNR values of CBI-interpolated abdominal slices versus linear method are plotted in Fig. 3.8 and the comparison in terms of relevance measure can be found in table 3.5.

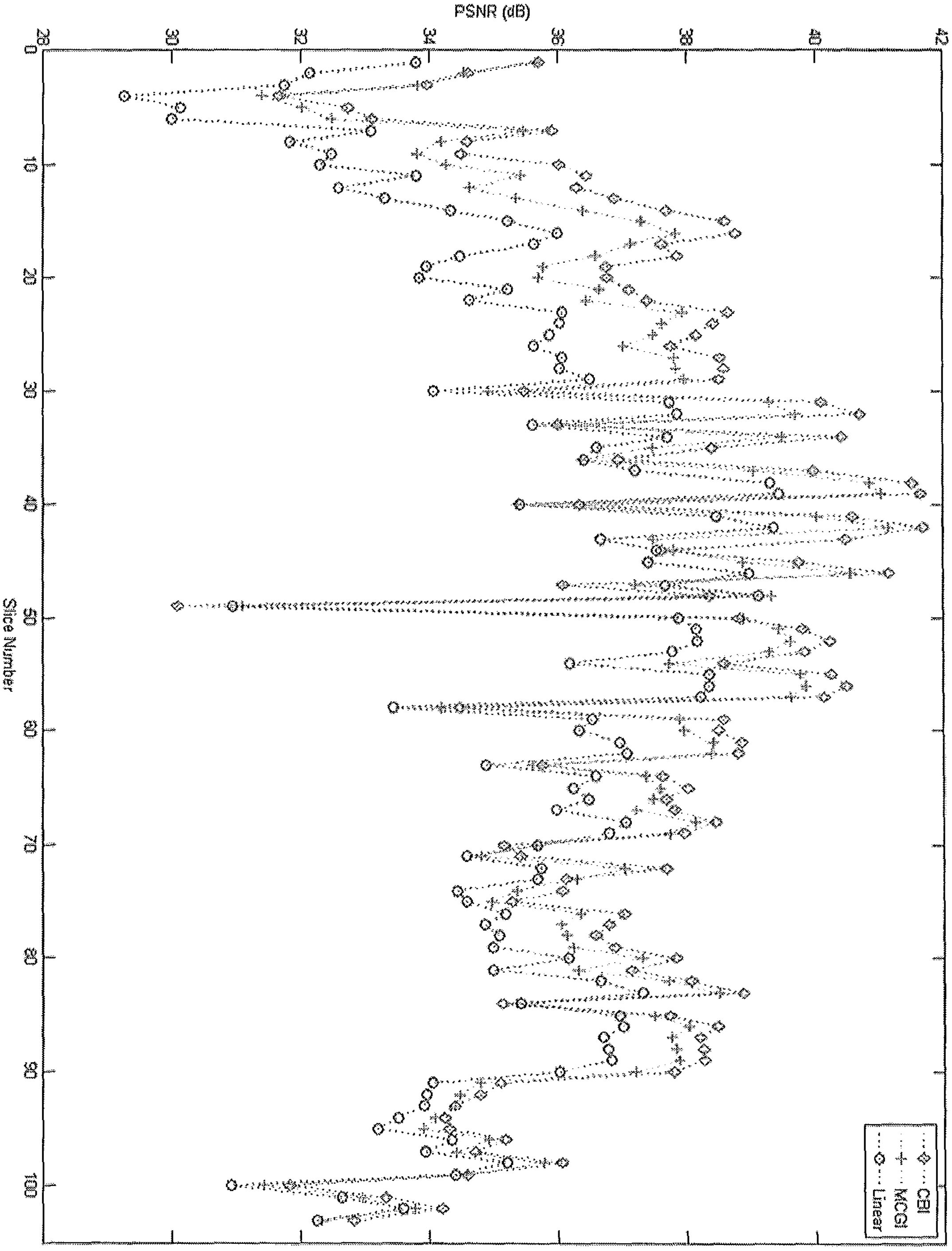

Figure 3.7: Interpolation of brain slices, CBI vs MCGI and linear

Table 3.4: Parameter of training set vs. test data for abdominal MRI

Data Class	Orientation	Ave No. of Slices	Slice Thickness	2-D Plane Size
Training Set	Axial	86	$4mm$	512×512
Test Sets	Axial	44	$8mm$	512×512

Table 3.5: Relevance measures for abdominal MRI

2-D Plane Size	$r_{mcgi/lin}$	$r_{cbi/lin}$
512×512	34.7	12.9

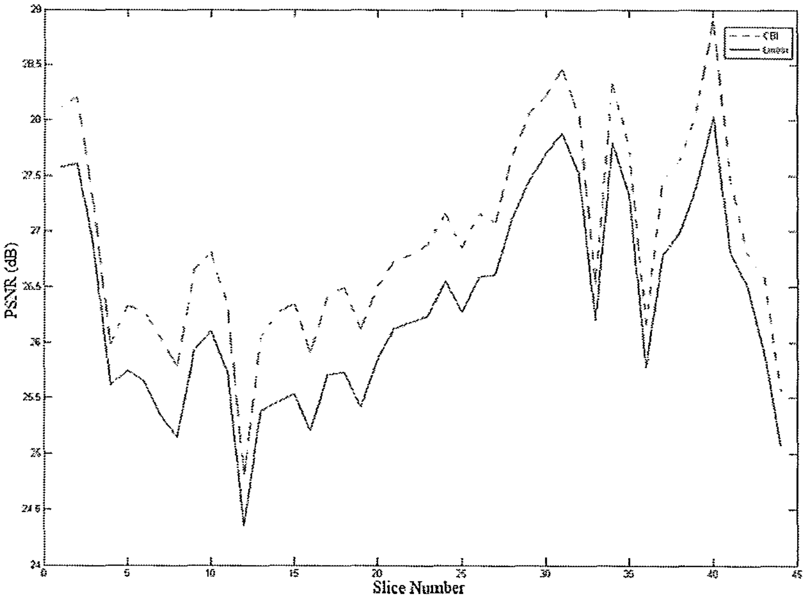

Figure 3.8: Interpolation of abdomen slices, CBI vs. linear

3.5 Conclusion

A novel context-based 3-D interpolation technique is proposed for medical applications. The technique allows the use of domain knowledge in estimating the missing voxels, adapts to local 3-D waveforms, and at the same time keeps the computational complexity low. Experimental results demonstrate the competitive performance of the proposed technique. The proposed method (CBI) shows significant improvement over the linear and MCGI methods for brain MR images. Comparing interpolated brain and abdomen images, the slice spacing of the training set is proved to be critical to the success of CBI. As the 2-D plane size decreases (Table 3.2) the superiority of CBI to MCGI, in terms of relevance measure, also decreases. This may be caused by the mismatch of slice size in training and test sets.

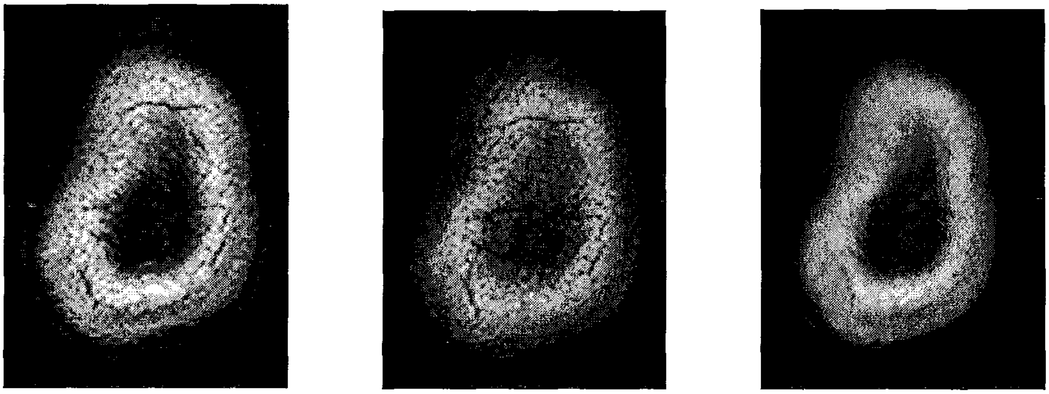

(a) Original (b) Linear (29.84 dB) (c) MCGI (32.00 dB)

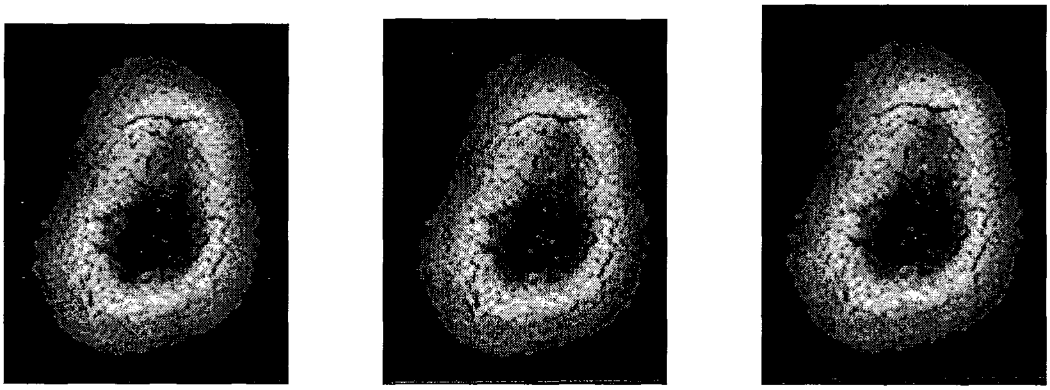

(d) CBI without ST (33.78 dB) (e) CBI, ST=T_1 (33.76 dB) (f) CBI ST=T_2 (33.71 dB)

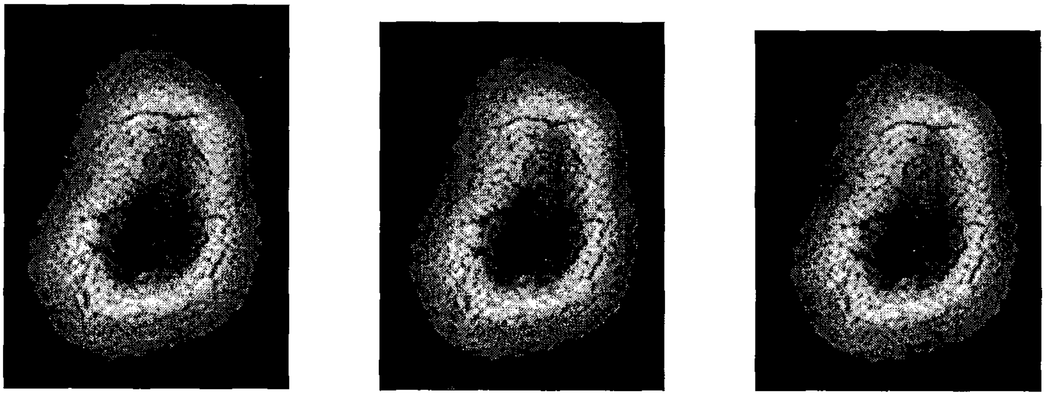

(g) CBI ST=T_3 (33.69 dB) (h) CBI ST=T_4 (33.68 dB) (i) CBI ST=T_5 (33.67 dB)

Figure 3.9: Visual comparison of different interpolation methods and different ST's for a T2 weighted image showing the skull

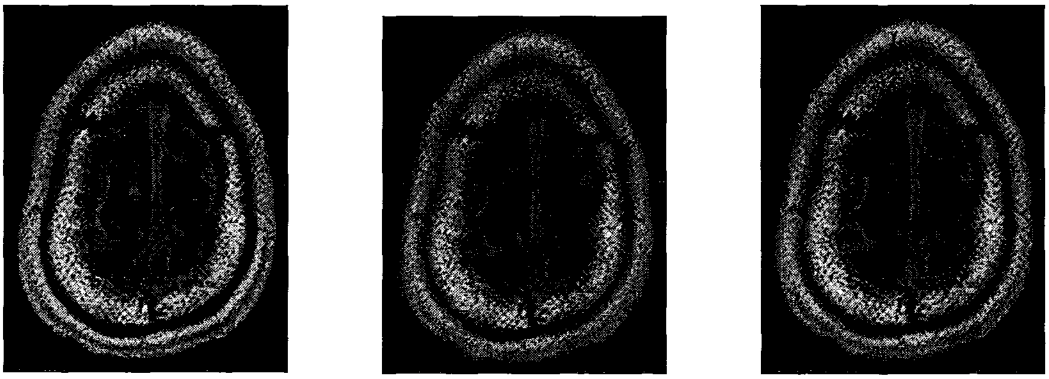

(a) Original (b) Linear (37.84 dB) (c) MCGI (39.69 dB)

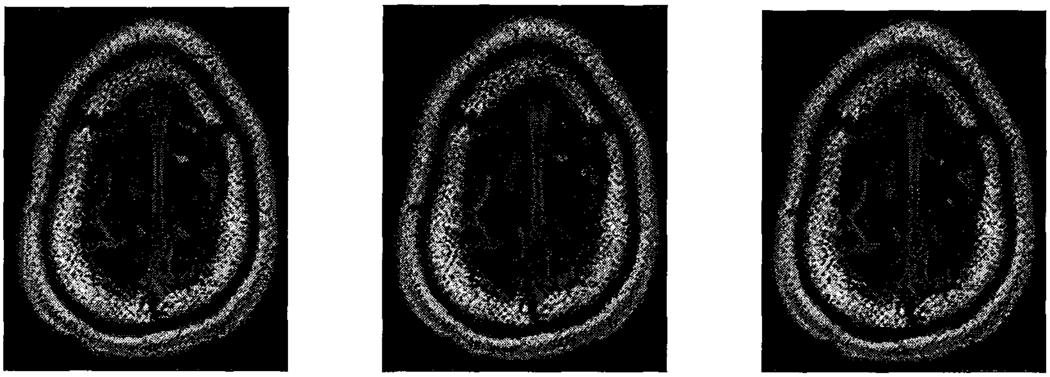

(d) CBI without ST (40.73 dB) (e) CBI, ST=T_1 (40.69 dB) (f) CBI, ST=T_2 (40.66 dB)

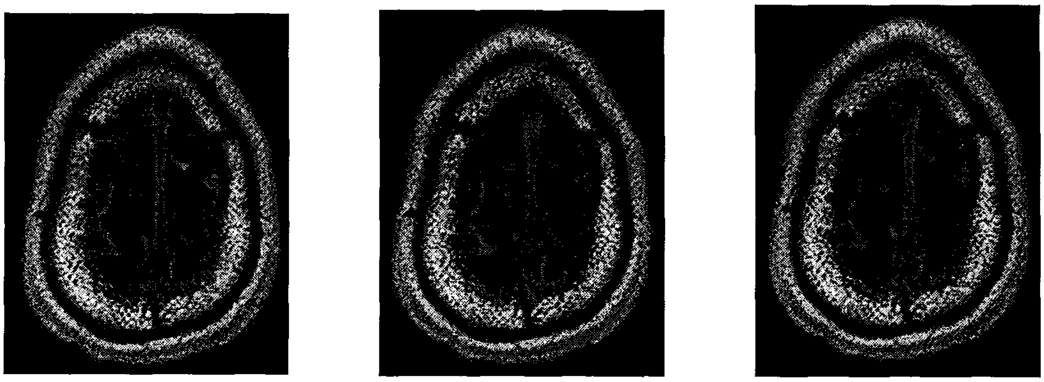

(g) CBI, ST=T_3 (40.64 dB) (h) CBI, ST=T_4 (40.60 dB) (i) CBI, ST=T_5 (40.53 dB)

Figure 3.10: Visual comparison of different interpolation methods and different ST's for a T2 weighted image showing the skull and hemispheres

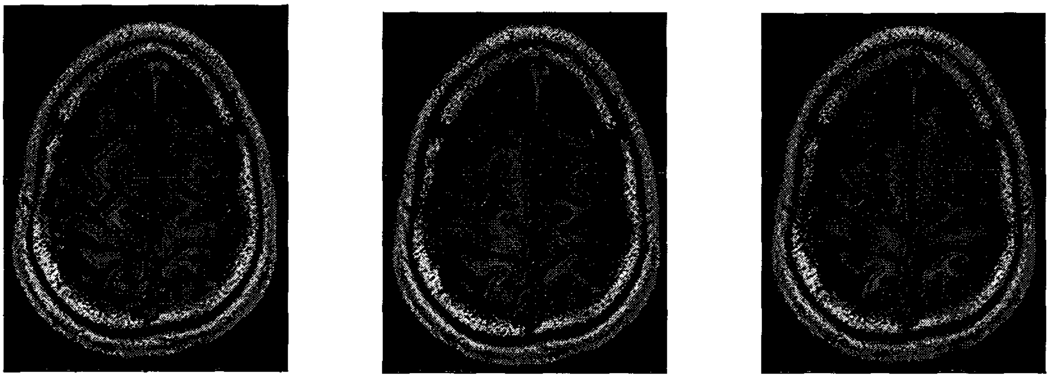

(a) Original (b) Linear (35.22 dB) (c) MCGI (37.29 dB)

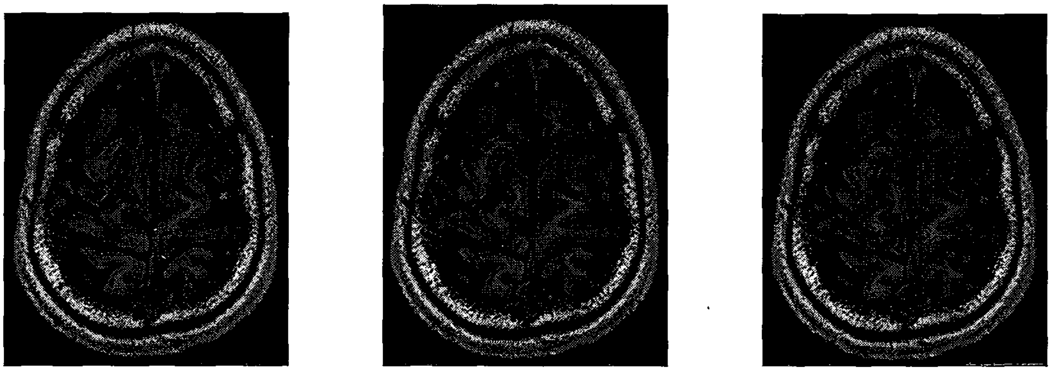

(d) CBI without ST (38.62 dB) (e) CBI , ST=T_1 (38.59 dB) (f) CBI , ST=T_2 (38.57 dB)

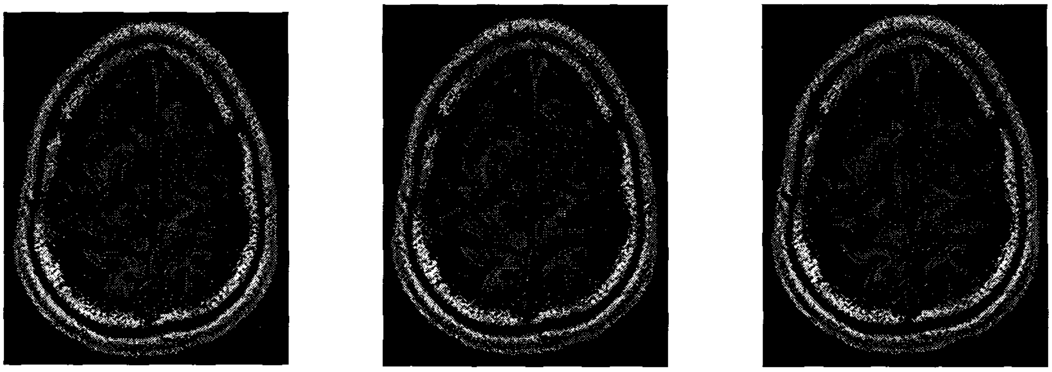

(g) CBI , ST=T_3 (38.56 dB) (h) CBI , ST=T_4 (38.53 dB) (i) CBI , ST=T_5 (38.50 dB)

Figure 3.11: Visual comparison of different interpolation methods and ST's for a T2 weighted image showing scalp fat, bone and hemispheres

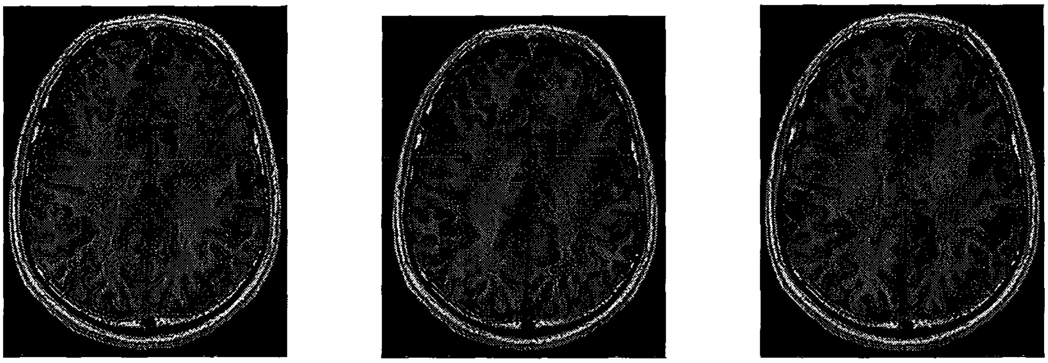

(a) Original (b) Linear (37.85 dB) (c) MCGI (39.69 dB)

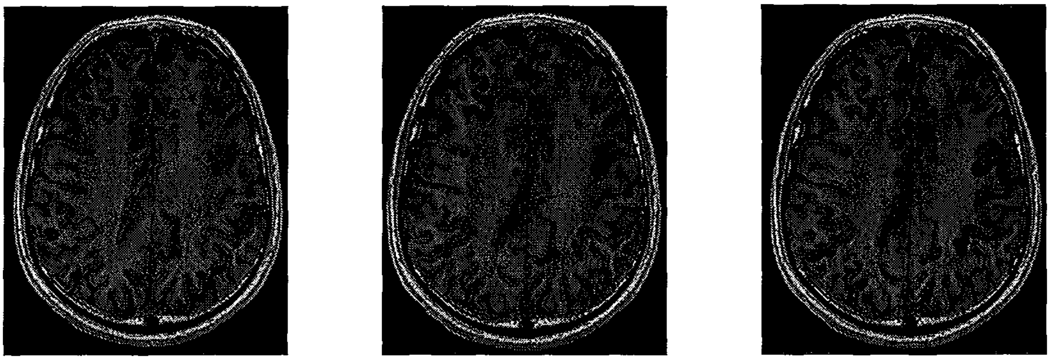

(d) CBI without ST (40.73 dB) (e) CBI , ST=T_1 (40.70 dB) (f) CBI , ST=T_2 (40.66 dB)

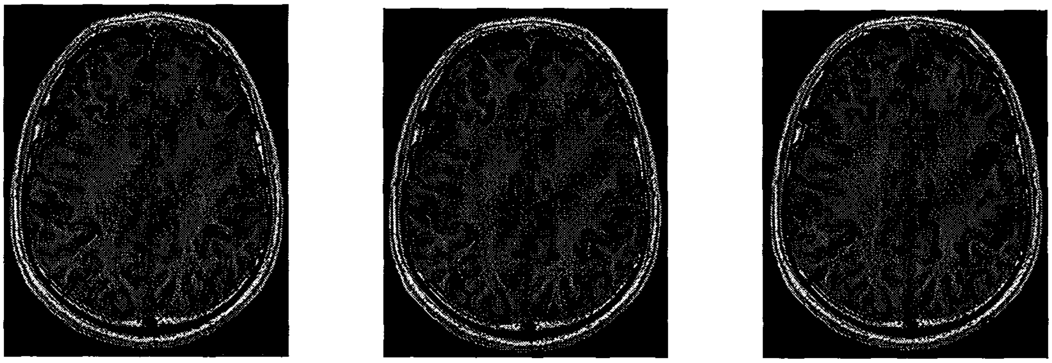

(g) CBI , ST=T_3 (40.65 dB) (h) CBI , ST=T_4 (40.61 dB) (i) CBI , ST=T_5 (40.53 dB)

Figure 3.12: Visual comparison of different interpolation methods and ST's for a T2 weighted image showing cortex, white and grey matter, and superior sagittal sinus

(a) Original (b) Linear (36.67 dB) (c) MCGI (37.49 dB)

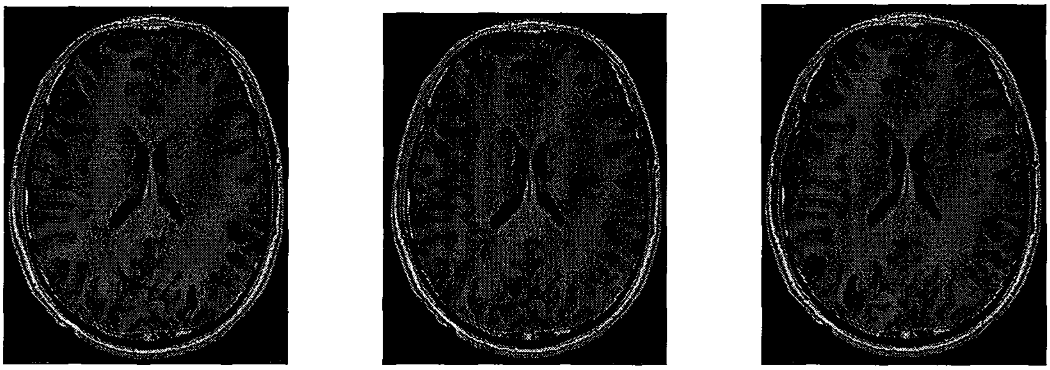

(d) CBI without ST (40.46 dB) (e) CBI , ST=T_1 (40.48 dB) (f) CBI , ST=T_2 (40.47 dB)

(g) CBI , ST=T_3 (40.34 dB) (h) CBI , ST=T_4 (39.62 dB) (i) CBI , ST=T_5 (38.69 dB)

Figure 3.13: Visual comparison of different interpolation methods and different ST's for a T2 weighted image showing cortex, lateral ventricle, and falx cerebri

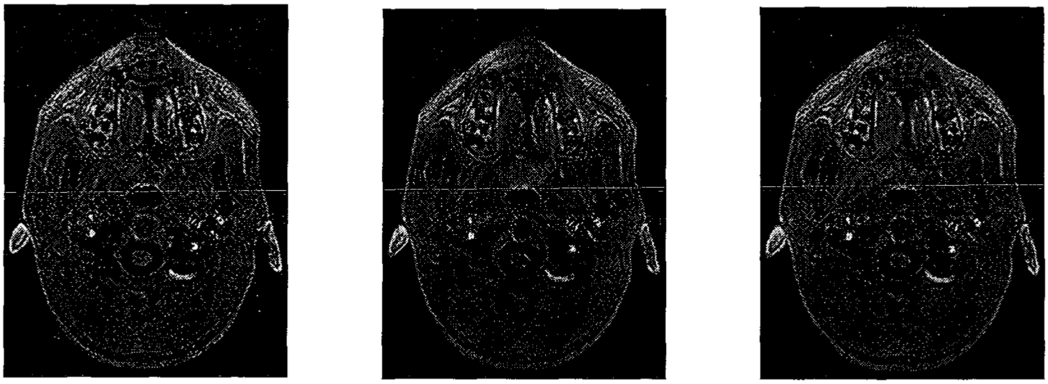

(a) Original (b) Linear (32.26 dB) (c) MCGI (32.32 dB)

(d) CBI without ST (32.84 dB) (e) CBI , ST=T_1 (32.84 dB) (f) CBI , ST=T_2 (32.81 dB)

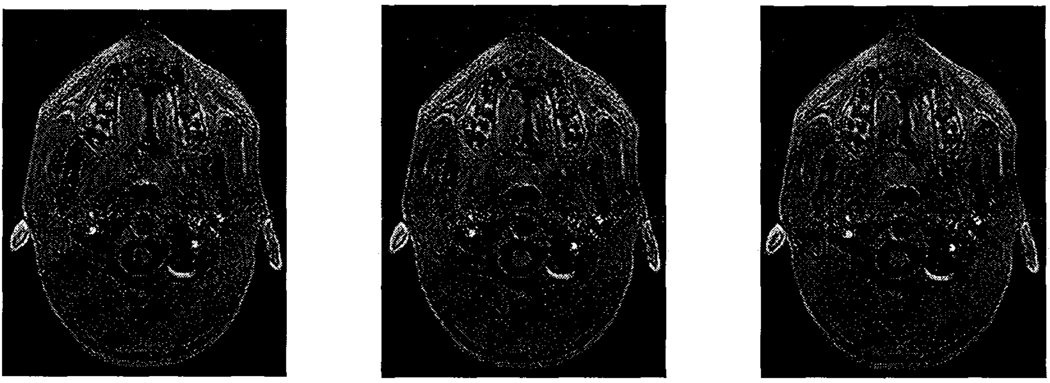

(g) CBI , ST=T_3 (32.74 dB) (h) CBI , ST=T_4 (32.64 dB) (i) CBI , ST=T_5 (32.57 dB)

Figure 3.14: Visual comparison of different interpolation methods and different ST's for a T2 weighted image showing the skull base starting at the cranial base

(a) CBI without ST (33.78 dB) (b) CBI ST=T_6 (33.66 dB)

Figure 3.15: Visual comparison of interpolation of an image featuring skull with no smoothness threshold and the least sensitive threshold (ST=T_6)

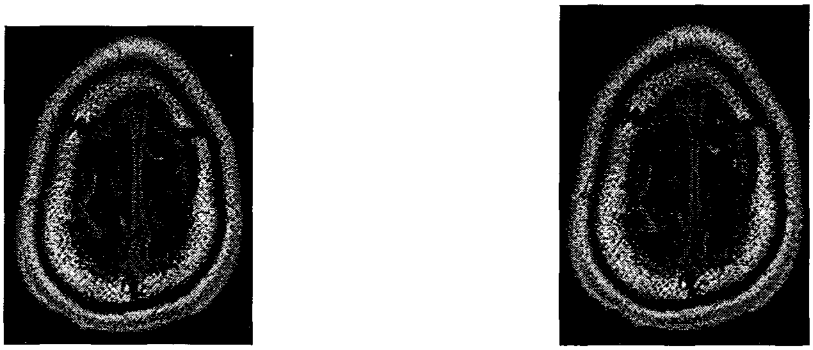

(a) CBI without ST (40.73 dB) (b) CBI, ST=T_6 (40.45 dB)

Figure 3.16: Visual comparison of interpolation of an image featuring skull and hemispheres with no smoothness threshold and the least sensitive threshold (ST=T_6)

(a) CBI without ST (38.62 dB) (b) CBI , ST=T_6 (38.46 dB)

Figure 3.17: Visual comparison of of interpolation of an image featuring scalp fat, bone and hemispheres with no smoothness threshold and the least sensitive threshold (ST=T_6)

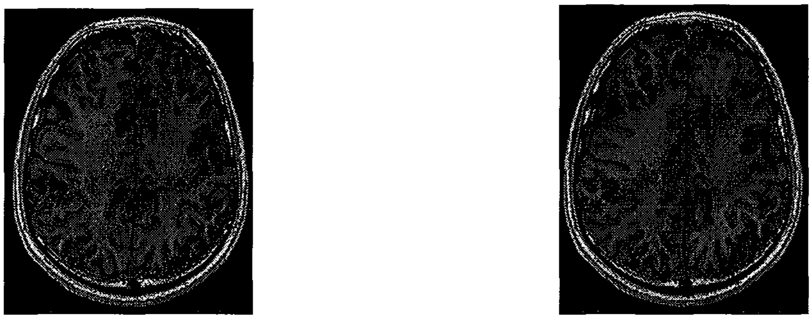

(a) CBI without ST (40.73 dB) (b) CBI , ST=T_6 (40.45 dB)

Figure 3.18: Visual comparison of interpolation of an image featuring cortex and sagittal sinus with no smoothness threshold and the least sensitive threshold (ST=T_6)

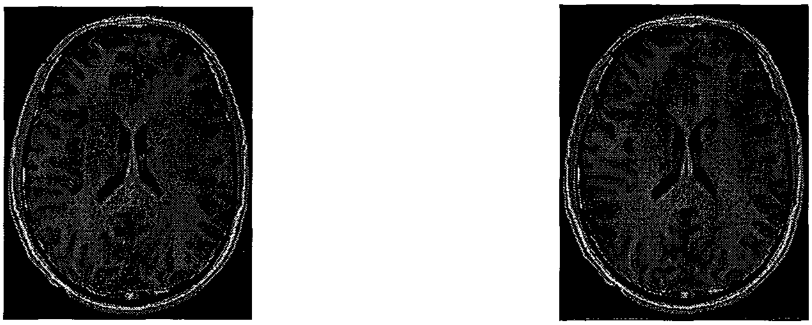

(a) CBI without ST (40.46 dB) (b) CBI , ST=T_6 (38.15 dB)

Figure 3.19: Visual comparison of interpolation of an image featuring cortex,lateral ventricle and flax cerebri with no smoothness threshold and the least sensitive threshold (ST=T_6)

(a) CBI without ST (32.84 dB) (b) CBI , ST=T_6 (32.53 dB)

Figure 3.20: Visual comparison of interpolation of an image featuring skull base with no smoothness threshold and the least sensitive threshold (ST=T_6)

Chapter 4

Concluding Remarks and Future Works

In this thesis we investigated the issue of non-isotropic medical image volumes and proposed two interpolation methods to overcome this shortcoming. The interpolation methods, PAR-based and CBI, both belong to adaptive interpolation class. Though the PAR-based method has been already validated in 2-D image interpolation, its performance, extended to 3-D, was not desirable; but it encouraged the initial idea for the latter method, CBI.

In CBI, the problem of slice up-conversion is aided by studying a training set. An HR set is used to determine statistical relations between the HR set and its corresponding LR set. In real-time applications, these statistical rules are employed to estimate the missing HR slices.

The second algorithm has been tested on a variety of brain MRI's of different patients and proved to outperform MCGI and linear methods. It has been also tested on some abdominal MRI's whose thickness is significantly greater than brain's. CBI showed superior performance to linear method; however MCGI works better for abdominal images. This could be due to the fact that MCGI is a motion compensating algorithm; it estimates the missing slice based on a motion field but switches to bicubic interpolator when the magnitude of the field is not very significant (the motion field increases as the slice spacing increases).

4.1 Future Works

Despite the fact that CBI method shows competitive performance compared to other interpolation approaches, there are some other issues that worth further investigation in the future. Some of them are outlined here:

1. In this work the training set parameters were confined to anatomy, modality and orientation. Future works may consider other parameters such as age, gender, slice size, ethnic background, etc.
2. The CBI method works better than MCGI for smaller slice spacing, while MCGI performs better as the slice spacing increases. The future works may design an interpolator that switches to optimal context-based interpolator or motion compensated interpolator based on the magnitude of the motion field. Alternatively, designing a context-based interpolator based on knowledge of motion field may also work similar to a switching interpolator.
3. A bigger motion field results in less accurate linear statistical rules. Higher order functions may establish more precise rules to relate the HR and LR sets.
4. Other approaches may be proposed to decrease algorithm run-time. Speed-up may be achieved by either a faster search method in online process or examining the training set to rule out areas where a non-adaptive interpolator performs satisfactory.

5. The applied clustering algorithm was k-means. Other clustering algorithms such as fuzzy clustering could be used in later works.
6. Different distance measures such as cosine, correlation, Mahalanobis, etc. could be utilized in clustering.
7. For optimal segmentation of a training set, some sophisticated shape detection algorithms can be used.

Bibliography

[1] A. P. Dhawan, *Medical Image Analysis*. Wiley Interscience, 1996.

[2] J. K. Udupa, “Display of 3d information in discrete 3d scenes produced by computerized tomography,” in *Proc. of IEEE*, pp. 420–434, 1983.

[3] G. J. Grevera and J. K. Udupa, “An objective comparison of 3-D image interpolation methods,” *IEEE Tran. Medical Imag.*, vol. 17, pp. 642–652, 1998.

[4] P. Thevenaz, T. Blu, and M. Unser, “Interpoaltion revisited,” *IEEE Tran. Medical Imag.*, vol. 19, pp. 739–758, 2000.

[5] T. M. Lehmann, C. Gonner, and K. Spitzer, “Survey: Interpolation methods in medical image processing,” *IEEE Tran. Medical Imag.*, vol. 18, pp. 1049–1074, 1999.

[6] G. T. Herman, S. W. Rowland, and M.-M. Yau, “A comparative study of the use of linear modified cubic spline interpolation for image processing,” *IEEE Tran. Nucl. Sci.*, vol. 26, pp. 2879–2894, 1979.

[7] R. G. Keys, “Cubic convolution interpolation for digital image processing,” *IEEE Trans. Acoust., Speech, Signal Processing*, vol. 29, pp. 1153–1160, 1981.

[8] M. R. Stytz and R. W. Parrot, "Using kriging for 3D medical imaging," *Computerized Med. Imag. and Graphics*, vol. 17, pp. 421–442, 1993.

[9] A. Goshtasby, D. A. Turner, and L. V. Ackerman, "Matching tomographic slices for interpolation," *IEEE Tran. Med. Imag.*, vol. 11, pp. 507–516, 1992.

[10] H. N. Christiansen and T. W. Sederberg, "Conversion of complex contour line definitions into polygonal element mosaics," *Comput. Graphics*, vol. 12, pp. 187–192, 1978.

[11] E. Aritz, G. Frieder, and G. Herman, "The theory. design, implementation and evaluation of a three-dimensional surface detection algorithm," *Comput. Graphics Image Proressing*, vol. 15, pp. 1–24, 1981.

[12] W. Lin, C. Liang, and C. Chen, "Dynamic elastic interpolation for 3-D medical image reconstruction from serial cross sections," *IEEE Tran. Medical Imag.*, vol. 7, pp. 225–232, 1988.

[13] S.-Y. Chen and W.-C. Lin, "Automated surface interpolation techniques for 3-D object reconstruction from serial cross-sections," *Comput. Med. Imag. Graph.*, vol. 15, pp. 265–276, 1991.

[14] C. Liang, W. Lin, and C. Chen, "Intensity interpolation for reconstructing 3-d medical images from serial cross-sections," in *Proc. IEEE Eng. in Medicine and Bilogy*, 1988.

[15] H. Fuchs, Z. M. Kedem, and S. P. Uselton, "Optimal surface reconstruction from plannar contours," *Commun. ACM*, vol. 20, pp. 693–702, 1977.

[16] G. Herman and C. Coin, "The use of 3D computer display in the study of disk disease," *J. Comput. Assist. Tomogr.*, vol. 4, pp. 564–567, 1980.

[17] R. Lu, P. Marziliano, and C. H. Thng, "Comparison of scene-based interpolation methods applied to ct abdominal images," in *Proc. Intl. Conf. IEEE EMBS*, pp. 1561–1564, 2005.

[18] S. P. Raya and J. K. Udupa, "Shape-based interpolation of multidimensional objects," *IEEE Tran. Medical Imag.*, vol. 17, pp. 642–652, 1990.

[19] J. Beutel, M. Sonka, and J. M. Fitzpatrick, *Handbook of medical imaging: Medical image processing and analysis*. SPIE, 2000.

[20] P. J. Taylor, *Distance transformation and distance decay functions*. University of Newcastle upon Tyne, Dept. of Geography, 1970.

[21] W. E. Higgins, C. Morice, and E. L. Ritman, "Shape-based interpolation of tree-like structures in three-dimensional images," *IEEE Tran. Medical Imag.*, vol. 12, pp. 439–450, 1993.

[22] G. T. Herman, J. Zheng, and C. A. Bucholtz, "Shape-based interpolation," *IEEE Tran. Medical Imag.*, vol. 12, pp. 69–79, 1992.

[23] J.-F. Guo, Y.-L. Cai, and Y.-P. Wang, "Morphology-based interpolation for 3-D medical image reconstruction," *Comput. Med. Imag. Graph.*, vol. 19, pp. 267–279, 1995.

[24] J. Goutsias and H. M. Heijmans, *Mathematical morphology*. IOS Press, 2000.

[25] T. Lee and W. Wang, "Morphology-based three-dimensional interpolation," *IEEE Tran. Med. Imag.*, vol. 19, pp. 711–721, 2000.

[26] V. Chatsiz and I. Pitas, "Interpolation of 3-D binary images based on morphological skeletonization," *IEEE Tran. Med. Imag.*, vol. 19, pp. 699–710, 2000.

[27] Y. Liu, Y. Sun, C. Mao, and C. Lin, "Edge-shrinking interpolation for medical images," *Comput. Vis., Graphics Image Processing*, vol. 21, pp. 91–101, 1997.

[28] G. P. Penny, J. A. Schnabel, D. Rueckert, M. A. Viergever, and W. J. Niessen, "Registration-based interpolation," *IEEE Tran. Med. Imag.*, vol. 23, pp. 922–926, 2004.

[29] G. J. Grevera and J. K. Udupa, "Shape-based interpolation of multidimensional grey-level images," *IEEE Tran. Med. Imag.*, vol. 15, pp. 881–892, 1996.

[30] T. Lee and C. Lin, "Feature-guided shpae-base image interpolation," *IEEE Tran. Med. Imag.*, vol. 21, pp. 1479–1489, 2002.

[31] T. Berier and Neely, "Feature-based image metamorphis," *Comput. Graphics SIGGRAPH*, vol. 26.

[32] D. Ruecker, L. I. Sonoda, C. Hayes, D. L. G. Hill, M. O. Leach, and D. J. Hawkes, "Nonrigid transformation using free-transform deformation: Application to breast MR images," *IEEE Tran. Med. Imag.*, vol. 18, pp. 712–721, 1999.

[33] D. H. Frakes, L. P. Dasi, K. Pekkan, H. D. Kitajima, K. Sundareswaran, A. P. Yoganathan, and M. T. Smith, "A new method for registration-based medical image interpolation," *IEEE Tran. Med. Imag.*, vol. 27, pp. 370–377, 2008.

[34] L. Torres and M. Kunt, *Video coding: the second generation approach.* Springer, 1996.

[35] X. Zhang and X. Wu, "Image interpolation by adaptive 2-D autoregressive modeling and soft decision estimation," *IEEE Trans. Imagage Processing*, pp. 887–893, 2008.

[36] X. Wu and N. Memno, “Context-based adaptive lossless image coding,” *IEEE Trans. Commun*, pp. 437–444, 1997.

[37] B. Meyer and P. Tischer, “TMWA new method for lossless image compression,” *presented at the Picture Coding Symp., Berlin, Germany*, 1997.

[38] A. Said and W. Pearlman, “An image multiresolution representation for lossless and lossy compression,” *IEEE Trans. Imagage Processing*, pp. 1303–1330, 1996.

[39] J. Sun, N. Zheng, H. Tao, and H. Shum, “Image hullucination with primal sketch priors,” *in IEEE Computer Society Conference on Computer Vision and Pattern Recognition*, pp. 729–736, 2003.

[40] X. Wu and X. Zhang, “Image interpolation using texture orientation map and kernel fisher discriminant,” in *Proc. Int. Conf. Image Processing*, pp. 49–51, 2005.